



Enhanced photo Fenton-like activity by effective and stable Al–Sm M-hexaferrite heterogenous catalyst magnetically detachable for methylene blue degradation

Ghulam Abbas Ashraf ^a, Raqiqa Tur Rasool ^b, Muhammad Hassan ^{c,*}, Lanting Zhang ^{a,**}

^a School of Materials Science and Engineering, Shanghai Jiao Tong University, 800 Dongchuan Road, Shanghai, 200240, China

^b School of Chemistry and Chemical Engineering (SCCE), Shanghai Jiao Tong University, 800 Dongchuan Road, Shanghai, 200240, China

^c School of Environmental Science and Engineering, Shanghai Jiao Tong University, 800 Dongchuan Road, Shanghai, 200240, China

ARTICLE INFO

Article history:

Received 25 August 2019

Received in revised form

18 November 2019

Accepted 15 December 2019

Available online 16 December 2019

Keywords:

Ba–Sr M-hexaferrites

Methylene blue

Photo-Fenton-like system

Heterogeneous photo-catalysts

Degradation pathway

ABSTRACT

Nano-compositing technologies are getting enhanced attention due to unique catalytic and separation activity with advanced characteristics for dye wastewater treatment. In this study, novel easily separable Ba–Sr based Al–Sm substituted M-hexaferrites (BASF-NPs) were fabricated as a highly effective heterogenous photo-Fenton-like catalysts via sol-gel route. The analytical techniques were applied to investigate BASF-NPs characteristics such as TGA, XRD, FTIR, XPS, SEM/TEM/EDS, UV–Vis, BET and VSM analysis. The results revealed that all fabricated BASF-NPs showed excellent photo-Fenton-like catalytic performance towards Methylene Blue (MB) degradation. Virtually complete degradation of an initial 10 mg/L MB was achieved under optimal conditions (i.e. 16 mM H₂O₂ and 0.25 g/L BASF-NPs) within 140 min of UV-irradiated reaction time and followed pseudo-first order reaction kinetic at the rate of $6.514 \times 10^{-2} \text{ min}^{-1}$. Similar degradation trend was noticed at various pH levels (pH 3–12), signifying the efficiency of the NPs at wide pH range. Due to the intrinsic magnetic nature of BASF-NPs, it was readily recoverable by external magnetic field and exposed strong capacity for dye removal treatment. The photo-catalysts retained its performance after four consecutive cycles, indicating robust reusability and excellent stability.

© 2019 Elsevier B.V. All rights reserved.

1. Introduction

The primary source of dye wastewater at large scale is manufacturing include industries of textile, paper, leather, cosmetic, food and paper that is highly dangerous for humans and environment, as it includes elevated dyes and a range of recalcitrant. For illustration, annually more than 100,000 commercially accessible dyes are manufactured worldwide at an approximate rate of over 7×10^5 tons. Due to the toxicity and carcinogenic nature character that eventually damage the human health and natural environment so the degradation of dyes in wastewater is a burning issue. The effective dye degradation methods like chemical oxidation, physical separation and biological degradation [1,2]. Advanced oxidation processes (AOPs) have presented excellent

potential for industrial waste water treatment among the various water treatment methods tested so far because hydroxyl radicals are extremely reactive species having 2.80 eV redox potential by adding H₂O₂ [3]. The produced hydroxyl radicals reacted with recalcitrant organic compounds as a consequence degradation of pollutants. The economical Fenton scheme (Fe²⁺ and H₂O₂) has substantial owing to generation of hydroxyl radicals ([•]OH) [4]. However, this traditional Fenton system has significant constrains, such as narrow pH < 3 range, high consumption of H₂O₂ and iron sludge produced as a binary pollution in treated waste water [5]. The heterogeneous (e.g. Fe₃O₄, γ-Fe₂O₃ and α-β-γ-FeOOH) Fenton catalysts typically have lesser activity in H₂O₂, due to the potential dissemination resistance of the reactants on the catalyst surface than the homogeneous counterpart. Additionally, in oxidation circumstances some catalysts possessed poor stability or durability due to metal leaching [6]. It is still necessary to develop efficient, stable, durable heterogenous catalysts to achieve a challenge.

Heterogeneous (HC) photo-Fenton-like systems are currently being researched as a more practical and effective alternative

* Corresponding author.

** Corresponding author.

E-mail addresses: m.hassan@sjtu.edu.cn (M. Hassan), lantingzh@sjtu.edu.cn (L. Zhang).

procedure for degrading recalcitrant organic pollutants. The magnetic materials required the characteristic like stability, reusability and high reactivity; can be functional in an extensive range of photo-decomposition of toxic and organic pollutants in wastewater [7]. In significance, various studies have been explored on HC photo-Fenton-like system using ferrites owing to their potential characteristics in the photo-degradation of different dyes. Andrei et al. [8] explored metal ions doped such as Co^{2+} , Mn^{2+} , Cu^{2+} and Ni^{2+} , MgFe_2O_4 nano-particles were applied as photo-Fenton-like catalysts for MB degradation in aqueous medium. Wang et al. [9] studied mesoporous copper substituted spinel ferrite HC Fenton-like system for imidacloprid degradation in existence of H_2O_2 . Xing et al. [10] studied Mg doped spinel ferrite with spherical nano-particles as HC Fenton-like system for dye removal. Strontium based M-hexaferrite ($\text{SrFe}_{12}\text{O}_{19}$) [11] was applied for the photo-catalytic removal of toluidine blue dye. Luna et al. [12] synthesized barium M-hexaferrite ($\text{BaFe}_{12}\text{O}_{19}$) with an application of HC photo-Fenton-like system for decolorization and mineralization of MB. Li et al. [13] used manganese substituted spinel ferrite HC catalysts with sphere-like particles as Fenton system for the dye degradation. Fatemeh et al. [14] fabricated with core shell structure Sr-M-hexaferrite@ SiO_2 @ TiO_2 composites with low degradation rate of MB under UV-irradiation. Guo et al. [15] prepared nickel substituted spinel ferrite with hollow sphere nano-particles which was applied as HC photo-Fenton catalysts for dye degradation. Rare earth cations like La and Ce substituted CoFe_2O_4 were explored by Rimi [16] for photo-Fenton activity. Similarly, Fe-based catalysts, such as Fe_2O_3 [17], Fe_3O_4 [18], α - FeOOH [19] and CuFe_2O_4 [20] have been used to stimulate H_2O_2 into reactive radicals for degradation of organic contaminants in water. Lili et al. [21] characterized copper doped AlPO_4 catalyst as a Fenton-like degradation in the existence of H_2O_2 at neutral pH.

However, Al–Sm substituted M-hexaferrite were rarely reported yet because of the key concern to improve catalytic activity of $\text{Ba}_{0.4}\text{Sr}_{0.6}\text{Al}_{0.4-x}\text{Sm}_x\text{Fe}_{11.60}\text{O}_{19}$ (Pure, $x = 0.0, 0.2, \text{ and } 0.4$) Ba–Sr based M-hexaferrite nano-particles henceforth named as BASF-NPs. Whereas, in M-hexaferrite, 24 Fe^{3+} ions, 38 O^{2-} ions and 2 M^{2+} ions are contained in unit cell, but Fe^{3+} ions are located at five locations ($4f_2$, $4f_1$, $2b$, $12k$ and $2a$), one site tetrahedral ($4f_1$), three sites octahedral ($4f_2$, $12k$, $2a$) and one site trigonal bipyramidal ($2b$). The sites of Fe^{3+} ions ($2a$, $2k$ and $2b$) and $4f_2$ and $4f_1$ are positioned with spin up and spin down direction, respectively. Fe^{3+} – O – Fe^{3+} are connected by aforementioned sites by super exchange interaction leading to ferromagnetic structure [22]. Al–Sm substituted having hexagonal structure shape, narrow energy band gap (E_g) and magnetic nature have turned out to be suitable material for environmental remediation. The synthesized hexaferrites catalysts have excellent diffusion efficiency and can be effectively and simply recovered by an external applied magnetic field for their ultimate reusability. As a result, the sustainability of superior active hexaferrite fulfills the green chemistry standards.

In this work, novel Al–Sm substituted M-hexaferrites (BASF-NPs) were fabricated by sol-gel method. This idea presents the application of BASF-NPs to elucidate as a HC photo-Fenton-like catalysts for MB degradation as a model bio-recalcitrant dye pollutant. The effects of BASF-NPs dosage, H_2O_2 concentration, and pH were evaluated. Reaction pathway was proposed based on the production of active intermediates during MB degradation process.

2. Experimental procedure

2.1. Chemicals

Methylene blue (MB, $\text{C}_{16}\text{H}_{18}\text{ClN}_3\text{S}\cdot 3\text{H}_2\text{O}$) (Macklin), ferric chloride ($\text{FeCl}_3\cdot 6\text{H}_2\text{O}$), strontium (II) nitrate: $\text{Sr}(\text{NO}_3)_2$, barium (II)

nitrate: $\text{Ba}(\text{NO}_3)_2$ (99%, Merck), samarium (III) oxide: Sm_2O_3 (99%, Aldrich), aluminum nitrate: $\text{Al}(\text{NO}_3)_3$, citric acid: $\text{C}_6\text{H}_8\text{O}_7$ and ammonium hydroxide: NH_4OH (99%, Aldrich) were utilized. All chemicals were of analytical grade and applied without further purification.

2.2. Synthesis of BASF-NPs

BASF-NPs were fabricated via sol-gel method. First, a distinct aqueous solution of FeCl_3 , $\text{Sr}(\text{NO}_3)_2$, $\text{Ba}(\text{NO}_3)_2$ and $\text{Al}(\text{NO}_3)_3$ of analytical grade according to stoichiometric calculation were equipped in deionized water for all metal ions precursors. For pure sample preparation the aqueous solution of FeCl_3 , $\text{Sr}(\text{NO}_3)_2$, $\text{Ba}(\text{NO}_3)_2$ were poured into baker and kept on stirring for 3 h at room temperature. In the meantime, $\text{C}_6\text{H}_8\text{O}_7$ to metal nitrates were engaged with 1:1 ratio, whereas NH_4OH solution was used to maintain the pH value ~ 7 – 8 for pure sample and others. For Al–Sm based samples fabrication, the aqueous of $\text{Sr}(\text{NO}_3)_2$, $\text{Ba}(\text{NO}_3)_2$ and $\text{Al}(\text{NO}_3)_3$, FeCl_3 and the measured quantity of Sm_2O_3 was liquefied in concentrated HNO_3 with constantly stirring at 80°C to produce $\text{Sm}(\text{NO}_3)_3$ then gradually transferred into solution. As the temperature steadily reached up to 120°C , the solution was more concentrated like a gel and obtained gel burned out, which was ground and further heated at 800°C for 3 h and 1100°C for 1 h to attain stable M-hexaferrite structure.

2.3. Characterization of BASF-NPs

In the ambient atmosphere, thermo gravimetry (TGA: NETZSCH STA 449) was performed with heating rate of 10°C per minute. BASF-NPs structure were recognized at room temperature by X-ray diffraction (D8 ADVANCE Da Vinci) with $\text{CuK}\alpha$ as the radiation source. The XRD pattern was recorded in the range of (20° – 85°) with scan rate 5° per minute. The FTIR spectra (Nicolet 6700) was recorded from 4000 to 350 cm^{-1} using the weight ratio of BASF-NPs and KBr (0.1:0.45), then mixed and ground in stainless steel die to make thin layer pellets at 27°C and 10 T. X-ray photoelectron spectroscopy (XPS; AXIS UltraDL) was conducted using Al $\text{K}\alpha$ as an exciting X-rays energy of 30 eV. Scanning electron microscope (SEM) and transmission electron microscopy (TEM) (Hitachi JEM) was employed to observe the size and morphology of BASF-NPs and elemental composition was detected by energy dispersive X-ray spectroscopy (EDS) (INCA X-Act). Before carrying out the SEM/EDS analysis, BASF-NPs were coated with gold particles. TEM study was equipped through carbon film copper grid method. UV–vis spectra were attained by UV-VIS, Lambda 750S spectrometer and from Kubelka–Munk method band gap was estimated. For the surface area and porosity assessment, Brunauer–Emmett–Teller (BET) surface analyzer (24/Autosorb-IQ3) was applied. At 77 K, nitrogen (N_2) isotherm gas adsorption was obtained. Before the test, BASF-NPs were outgassed at 424 K under vacuum. Magnetic performance was explored by applying the magnetometer (VSM, Quantum Design PPMS-9T EC-II) at room temperature within range -15 kOe to 15 kOe.

2.4. Photo degradation experiments

A 10 mg/L MB dye was used in a desired amount of distilled water solvent under photo irradiation sourced by low pressure mercury lamp (UV; 10 W) and inserted into the lab designed photo-reactor with displacement volume of 1 L (Fig. 1). To prevent from the surround light intact, the reactor was coated with tinfoil. Various BASF-NPs doses and H_2O_2 concentrations were applied ranging from 0.00 to 1.00 g/L and 4–16 mM, respectively for

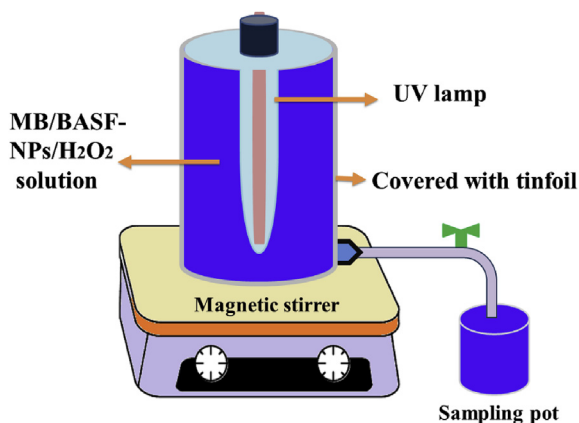


Fig. 1. Experimental assembly.

optimization during 140 min reaction time. The sample was taken every 20 min interval from photo-reactor. BASF-NPs were separated by applying external magnetic effect and then filtered the solution through 0.2 μm syringe filters. The filtered solution was examined using double-beam UV–Vis spectrophotometers (UV-VIS, Lambda 750 S) within wavelength of 400–700 nm. The achieved optimal condition such as such as 0.25 g/L BASF-NPs and 16 mM H_2O_2 were further used to explore the impact of various pH (3, 7 and 12 with HCl or NaOH) and also changing the primary MB concentration (10, 20 and 30 mg/L) on MB degradation. The degradation percentage of MB was achieved by:

$$\text{MB Degradation} = \frac{(C_0 - C_t)}{C_0} \times 100\% \quad (1)$$

whereas, C_0 = initial and C_t = after t time concentration of MB. Total organic carbon (TOC) (TOC-5050, Shimadzu, Japan) tracked the degree of MB mineralization. The level of metallic ions leaching was evaluated with inductive coupled plasma optical (ICAP7600). For the detection of hydroxyl radicals ($\cdot\text{OH}$) fluorescence spectrophotometer (RF-5301-PC-Shimadzu) was employed. Liquid chromatography attached with tandem mass spectrometer (UPLC-MS) evaluated the photo-degraded intermediates of MB. The study of recyclability and stability were explored as the recovered photocatalyst from solution by a bar-magnet, washed with water, dried then spread over in the next cycles with same conditions.

3. Results and discussions

3.1. Characteristics of BASF-NPs

As shown in Fig. 2 the clear hexaferrite structure formation occurred through TGA/DSC curves from room temperature to 1200 $^\circ\text{C}$. At 150 $^\circ\text{C}$ the endothermic (TGA) curve was observed due to the weight loss of hydrated water from dried sample. In the second portion of temperature range from 200 to 850 $^\circ\text{C}$ was associated with the decomposition of metal hydroxides in their respective metal oxide and loss of NH_3 gas [23]. In addition, the larger weight loss in the second portion of exothermic peaks tend to show the response of nitrates and citric acid that eventually formed metal oxides. The endothermic peaks from 300 to 850 $^\circ\text{C}$ display that the decomposition of unreacted citric acid. Indeed, growth of grain and nucleation can be achieved from amorphous to hexagonal where the weight loss can be stable. For the achievement of hexagonal phase, the dried gel was calcinated for 3 h at 800 $^\circ\text{C}$ and 1 h at 1100 $^\circ\text{C}$ [24,25].

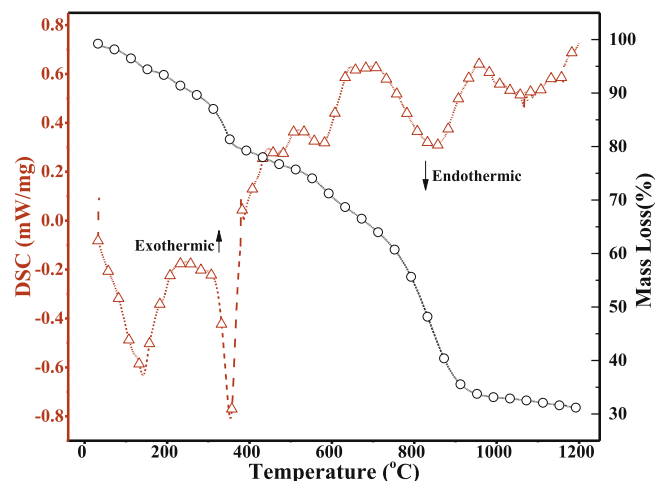


Fig. 2. TGA/DSC analysis of BASF-NPs ($x = 0.1$).

BASF-NPs crystal structure is composed in between oxygen ions (O^{2-}) and metal ions such as Fe^{3+} and Me^{3+} as metal substituted ions. XRD patterns were evaluated for M-hexaferrites to examine the hexagonal phase as presented in Fig. 3. There is a strong indication of hexagonal M-type structure with space group $\text{P6}_3/\text{mmc}$ (194) and having standard JCPDS file no. 51–1879 which is inserted in Fig. 3 for comparison. It appears that XRD pattern demonstrate minor $\alpha\text{-Fe}_2\text{O}_3$ secondary phase having JCPDS file number 00-033-0664. In addition, Sm^{3+} substitution ($0.2 \leq x \leq 0.4$) caused another minor phase FeSmO_3 having JCPDS file number 00-039-1490 as well as minor $\alpha\text{-Fe}_2\text{O}_3$ secondary phase. While pure M-hexaferrite ($\text{Ba}_{0.4}\text{Sr}_{0.6}\text{Fe}_{12}\text{O}_{19}$) depicted obviously identical results as described by Iqbal et al. [26]. The lattice parameters a (5.885 to 5.891 \AA) and c (23.085 to 23.106 \AA) depicted the slight variation in the crystal structure due to the Al–Sm substitution at Fe site [27,28]. By using the Debye-Scherrer eq. (2), the crystallite size (D_{xrd}) was evaluated:

$$D_{\text{xrd}} = \frac{0.9\lambda}{\beta_{\frac{1}{2}} \cos \theta} \quad (2)$$

whereas, D_{xrd} = average crystallite size, θ = Bragg angle (degree), $\lambda = 1.5406 \text{\AA}$ and β = full wave at half maximum (FWHM). Hence, D_{xrd} of BASF-NPs is within range (39.47–45.49 nm) which is well matched [29].

The FTIR spectra of the synthesized BASF-NPs is shown in Fig. 4. The wavenumber range extended from 4000 to 350 (cm^{-1}). The existence of two absorption band around 452.74 and 596.58 (cm^{-1}) are attributed to the stretching vibration of M–O bond (metal–oxygen) [30]. No absorption in the range of 1000–3500 cm^{-1} could be attributed to the absence of residual (metal carbonate), nitrates and

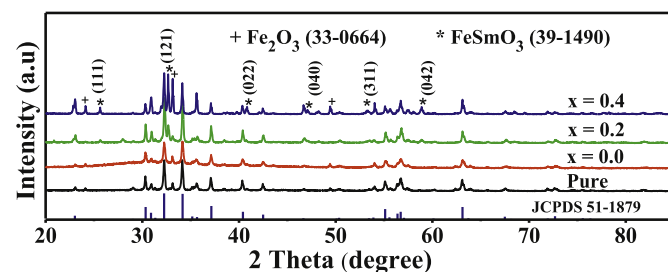


Fig. 3. XRD pattern of BASF-NPs. (pure sample; $\text{Ba}_{0.4}\text{Sr}_{0.6}\text{Fe}_{12}\text{O}_{19}$, $x = 0.0, 0.2$ and 0.4).

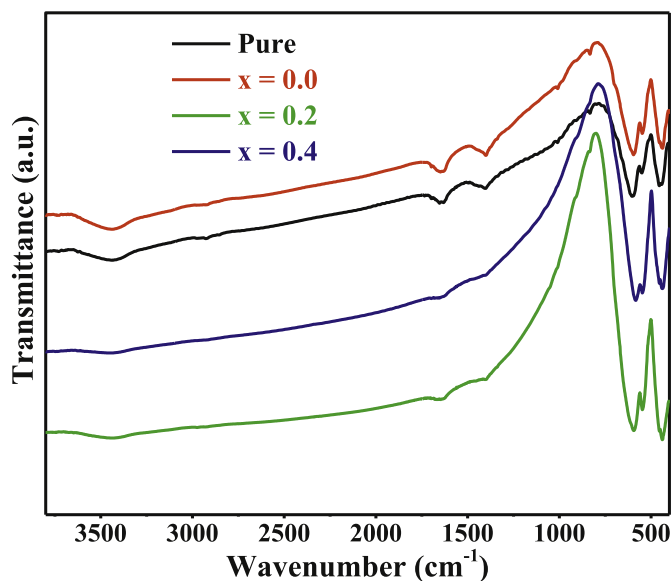


Fig. 4. FTIR spectra of BASF-NPs.

residual water stretching vibration, signifying that water residues, carbon and nitrates were totally burned off by self-ignition. The appearance of absorption in $434\text{--}443\text{ cm}^{-1}$ (ν_2) band range ascribed to Fe–O bending vibrations of Fe–O₄ and stretching vibrations of Fe–O₆, while the Fe–O stretching vibrations of Fe–O₄ ascribes in range $580\text{--}597\text{ cm}^{-1}$ (ν_1) [31]. Moreover, a slight shift of bands (ν_1 and ν_2) to low frequency occurred with increasing Sm³⁺ and decrease in Al³⁺ contents (x).

XPS was used for the oxidation states of elements in BASF-NPs. As shown Fig. 5 (a), from the XPS spectrum (from 1200 to 10 eV) of BASF-NPs (x = 0.2) surface consists of Ba, Sr, Al, Sm, Fe and O elements. As illustrated in Fig. 5 (b) Ba²⁺ 3d XPS spectra possessed binding energies of Ba 3d_{5/2} (780.4 eV) and Ba 3d_{3/2} (795.7 eV). The strontium Sr²⁺ 3d two positioned around 134.4 eV (Sr 3d_{5/2}) and 136.2 (Sr 3d_{3/2}) eV agreeing to the photo-electron peaks (Fig. 5 (c)) [32,33]. The spectra of Fe³⁺ 2p_{1/2} (720 eV) and Fe²⁺ 2p_{3/2} (711.6 eV) is presented in Fig. 5 (d), Al binding energy located around 73.9–74.9 eV which is well matched [34]. The Sm³⁺ 3d_{3/2} binding energy was 1083.8 eV [35,46] which is depicted Fig. 5 (e).

SEM observed the surface and microstructure of BASF-NPs as depicted in Fig. 6. By implementing line intersection method on each SEM image, the grain size of BASF-NPs was deliberated. It is found that the average grain was within range of 1.20–0.50 μm . The observed morphology of grains shape is seemed to be irregular platelet-like hexagonal [36,37]. The size of grain is increased up to x = 0.4 as the Sm contents increased and the grain shape is appeared spherical. The increasing grain size might be associated with substituted Sm³⁺ ions in hexaferrite system having larger atomic size which repositioned on grain boundaries [38]. EDS was used to acquire BASF-NPs from a quantitative energy dispersive spectrum. It is obviously disclosed in a possible error range about 10% for all related peaks of BASF-NPs elements like as strontium (Sr), barium (Ba), iron (Fe), samarium (Sm), aluminum (Al) and oxygen (O). Sr, Ba Sm, Al, Fe and O are elemental mapping of all noticed elements in EDX spectroscopy, which clearly specify the homogeneous elemental distributions as presented in Fig. S1. TEM explored the morphology in order to get clearer perspective of BASF-NPs for pure and x = 0.2) samples. The 3D grain shape is presented in Fig. 7 (c). As observed in Fig. 7 BASF-NPs are platelet-like hexagonal structure. The results of XRD and TEM confirmed that BASF-NPs composites was successfully fabricated.

UV–Vis spectra were employed to investigate BASF-NPs optical absorption properties. Optical band gaps (E_g) in semiconductor type materials are significant consideration during photo-degradation. As the narrow E_g leads to elevated solar photon absorption effectiveness. The absorption band is linked to electron excitation from valance to conduction band, that determines E_g features. The absorption spectra and $(\alpha h\nu)^2$ vs $h\nu$ (eV) of BASF-NPs were calculated, as shown in Fig. 8 (a) and (b) respectively. In a Tauc equation (3), energy of the incident photon ($h\nu$) and absorption coefficient α :

$$\alpha h\nu = A(h\nu - E_g)^{1/2} \quad (3)$$

whereas, A = constant value and E_g = energy band gap. BASF-NPs' Tauc graph with measured E_g values as presented in Fig. 8 (b). For E_g values a tangent line was calculated to bisect the horizontal x-axis which crossed the absorption curve at the point of inflection, and the values were found to be 1.65 eV, 1.68 eV, 1.74 eV and 1.85 eV for pure sample, BASF-NPs (x = 0.0, 0.2 and 0.4), respectively. It was seen from Fig. 8 (b) that E_g values increase by Al–Sm substitution, suggesting the role of substituents in altering the basic lattice structure. It can be attributed to the quantum confinement effect which is corroborated with shape and size of the grains [39,40]. Luna and Wang et al. [12,37] reported E_g ; 1.77 eV and 1.70 eV for barium hexaferrite, correspondingly. Furthermore, the narrowband gap of substituted M-hexaferrites enhanced the visible-light absorption.

The porous behavior of BASF-NPs are evaluated by adsorption-desorption isotherms analysis as shown in Fig. 9. The catalyst's activity primarily depends on the surface area. It is ascribed to larger surface area of nano-particles that provides more active surface for photo-catalytic response. BET surface analyzer was applied to explore the surface area of pure sample at 77 K. Sample testing was initially performed with N₂ gas stream at 150 °C for 2 h. Fig. 9 (a) illustrates the specific curves of adsorption-desorption with relatively pore sizes of BASF-NPs. The surface area of pure, x = 0.0, 0.2 and 0.4 were noted as 5.85, 5.44, 8.26, 5.90 m²/g; its pore volume was approximately 0.007, 0.014, 0.059, 0.025 cc/g, respectively as shown in Fig. 9 (b), according to BJH desorption summary. During photo Fenton-like catalysis, the well-grown porosity and larger surface area of the catalyst allow contaminants to boost catalytic efficiency [41].

M-H loops of BASF-NPs were calculated at room temperature within applied magnetic field –15 kOe to 15 kOe (Fig. 10 (a)). The magnetic features are measured as summarized in Table S1 from M-H loops. The varying saturation magnetization (M_s) values are linked to different cationic position in unit cell of M-hexagonal ferrite. The declining trend of M_s is correlated to the substituted non-magnetic ions. Non-magnetic having large sized substituted ions prefer octahedral sites like $4f_2$, $2a$ and $12k$ in M-hexaferrites system [42]. Al³⁺ ions are preferred at following sites $4f_2$, $4f_1$ and $12k$ which decreased the M_s at x = 0.0. As the substitution contents of Sm³⁺ ions increased up to x = 0.2 and increase of M_s might be ascribed to occupancy at A-site. The Sm³⁺ ions have lesser magnetic moment than Fe³⁺ ions [43] whereas, the maximum Sm³⁺ ions substitution at x = 0.4 caused in declining of M_s because of the reduction of magnetization of B sub lattice by Sm³⁺ ions [43].

The coercivity (H_c) is an intrinsic and extrinsic feature that is reliant on shape and size of crystalline, microstructure and cations distribution. The significant decreasing trend of H_c due to magneto crystalline anisotropy was observed by the substituted Al–Sm ions at Fe site as presented in Table S1. H_c is proportionally dependent on anisotropy field H_a . The substituent and host ionic radii play a significant role whereas, Sm³⁺ ions have larger ionic radii than Fe³⁺

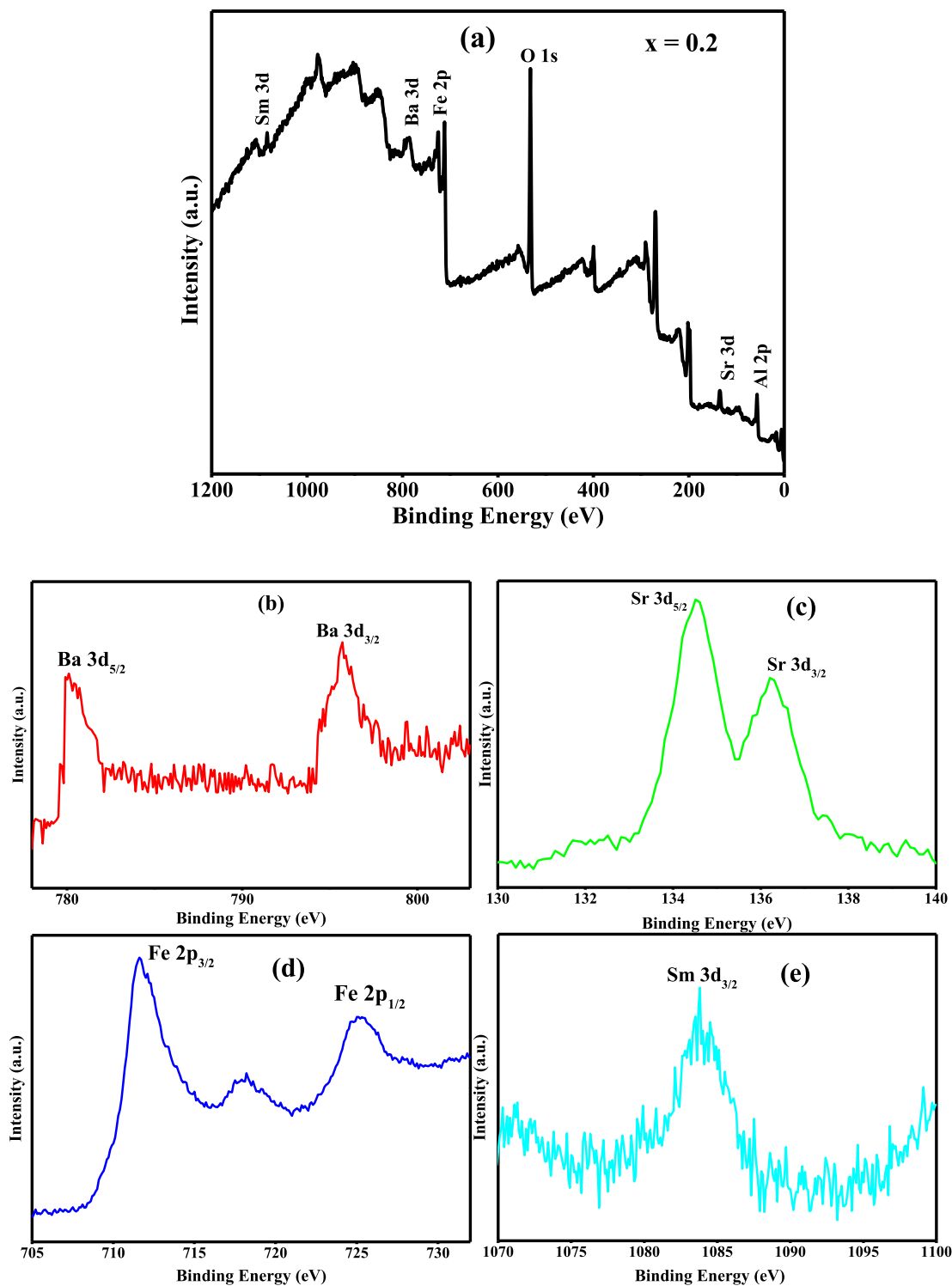


Fig. 5. XPS spectrum of BASF-NPs ($x = 0.2$).

ions. H_c is inversely proportional to grain size of M-hexaferrites as the grain size was observed larger with substitution (x) as shown in Table S1. The existence of impurity phases such as Fe_2O_3 and $FeSmO_3$ impacted so, H_c (Oe) is decreased while M_s (emu/g) increased at $x = 0.2$ and then decreases as the amount of Sm increased as reported in literature [44,45]. M-hexaferrite catalyst was effectively isolated after MB degradation with an external applied magnetic field as presented in Fig. 10 (b).

3.2. Photo-catalytic activity of MB

3.2.1. Photo-catalyst dosage

The selected dosage of BASF-NPs ($x = 0.0$) are consumed from 0.00 g/L to 1 g/L with constant concentration of dye 10 mg/L (MB) in photo-degradation system. MB degradation performance of the photo-catalyst without hexaferrite (0.00 g/L) showed a slight shift in MB concentration. It is ascribed to photolysis degradation. The

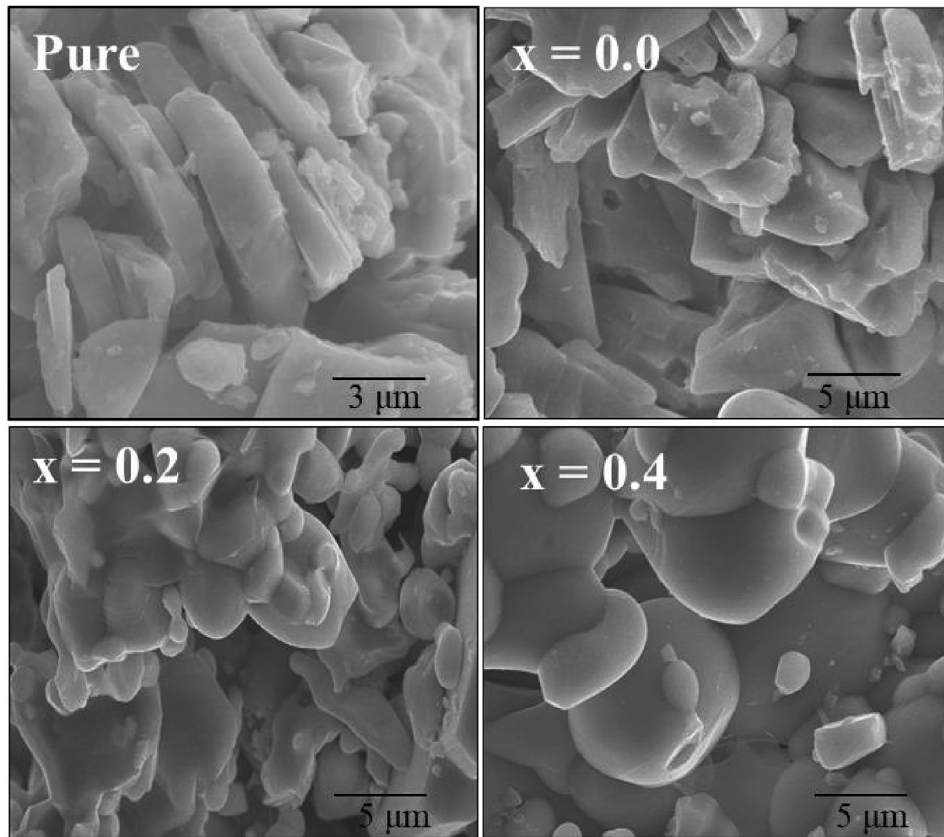


Fig. 6. SEM micrographs of BASF-NPs (pure sample: $\text{Ba}_{0.4}\text{Sr}_{0.6}\text{Fe}_{12}\text{O}_{19}$, $x = 0.0, 0.2$ and 0.4).

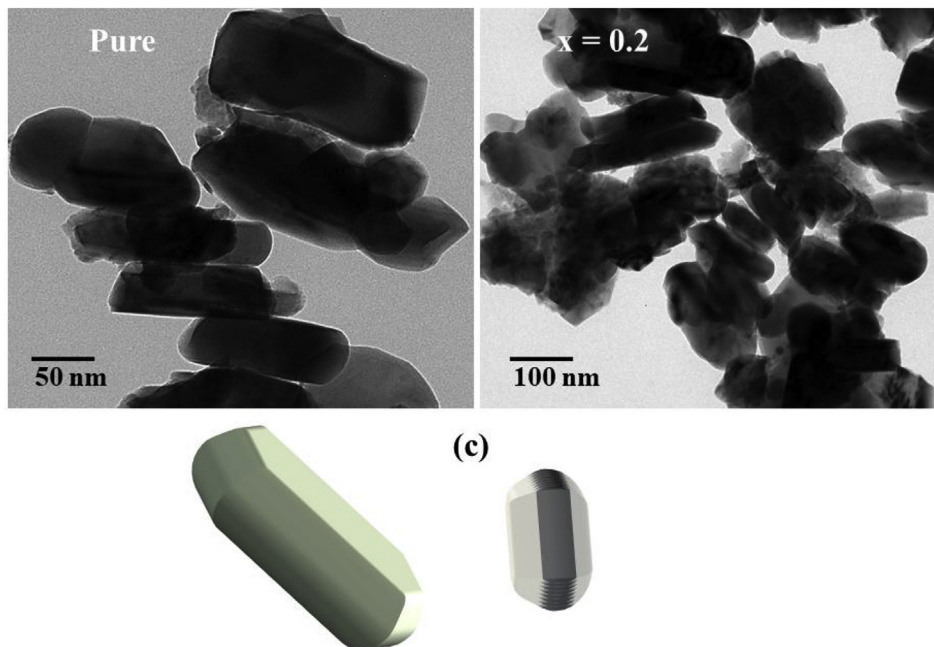


Fig. 7. TEM micrographs of BASF-NPs (pure sample: $\text{Ba}_{0.4}\text{Sr}_{0.6}\text{Fe}_{12}\text{O}_{19}$ and $x = 0.2$) and (c) 3D view of particles.

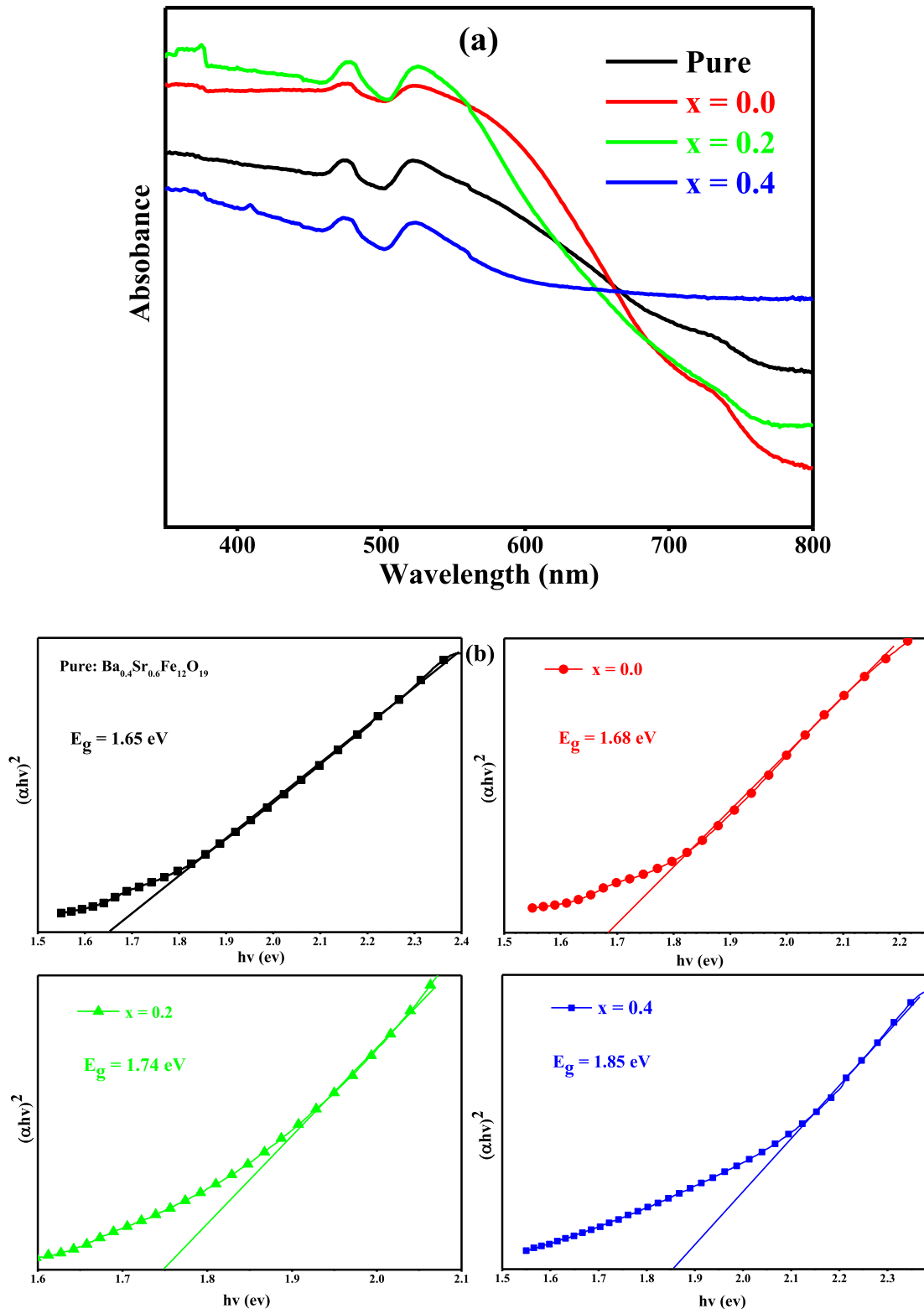


Fig. 8. (a) UV-Vis spectra of BASF-NPs (b) Tauc's plots of $(\alpha h\nu)^2$ versus photon energy for band gap energy of pure sample, $x = 0.0, 0.2$ and 0.4 (BASF-NPs).

concentration of BASF-NPs was increased from 0.50 to 1 g/L as a result degradation of MB was decreased which is due to the filter blocking effect by passage of light in reaction with reaction rate constant k from 0.0356 to $0.0292 \times 10^{-2} \text{ min}^{-1}$. However, the more catalyst was created to reduce light transmittance in solution, the

alternative was declined the production rate of active species [47]. M-hexaferrite (BASF-NPs) exhibited optimum catalyst concentration of 0.25 g/L about 39% degradation of MB after 140 min by photolysis. Thus, the optimal concentration of BASF-NPs was determined 0.25 g/L at natural pH (7) as revealed in Fig. 11. (a).

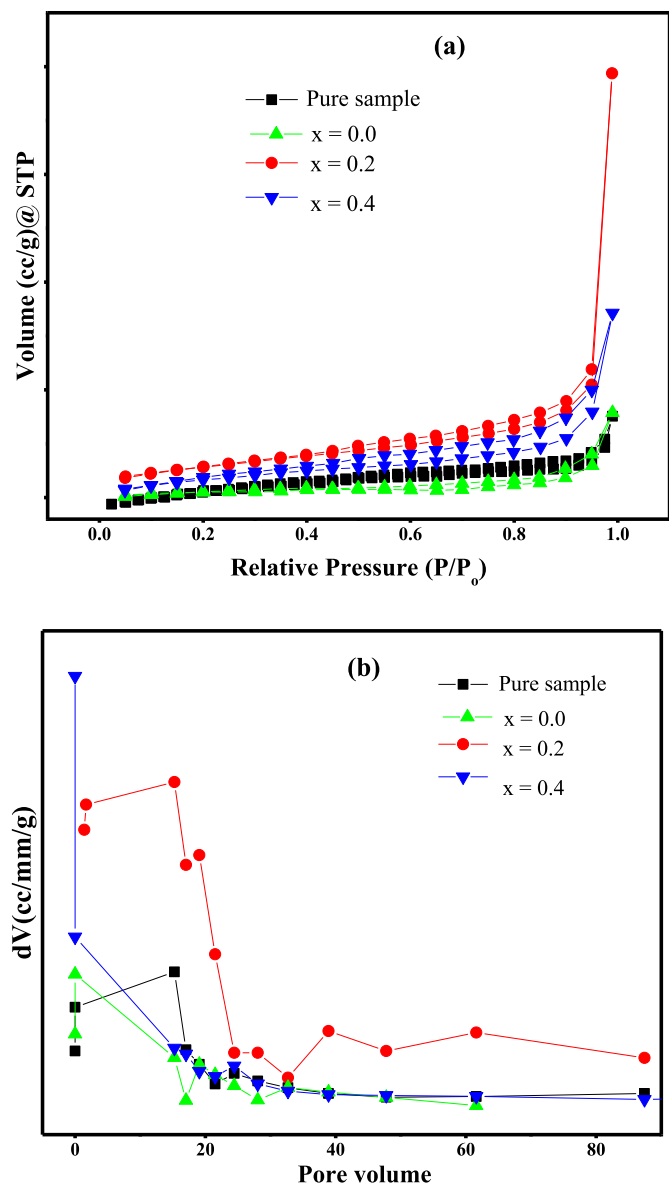


Fig. 9. (a) Isotherms of adsorption-desorption nitrogen (N₂) and (b) pore volume of pure sample, x = 0.0, 0.2 and 0.4 (BASF-NPs).

The closely-fitted lines in Fig. 11. (b) revealing a high linearity ($R^2 = 0.99$) indicated that MB degradation followed pseudo-first-order kinetics during photolysis, which can be stated in Eq. (4) [48];

$$-\ln\left(\frac{C_t}{C_0}\right) = kt \quad (4)$$

where, C_0 = initial concentration, C_t = after time (t) concentration of MB, t = irradiation time (min) and k (min^{-1}) is the rate constant of first order reaction. The rate constant (k value) for various concentration of hexaferrite are presented in Fig. 11. (c). The maximum k value of $0.0292 \times 10^{-2} \text{ min}^{-1}$ was obtained at 0.25 g/L M-hexaferrite dosage removing 39% of MB concentration. Therefore, 0.25 g/L BASF-NPs dosage was chosen for further studies.

3.2.2. Concentration effect of H₂O₂

H₂O₂ concentration is crucial for the Fenton and photo-Fenton-like system. Several H₂O₂ concentrations were used in this

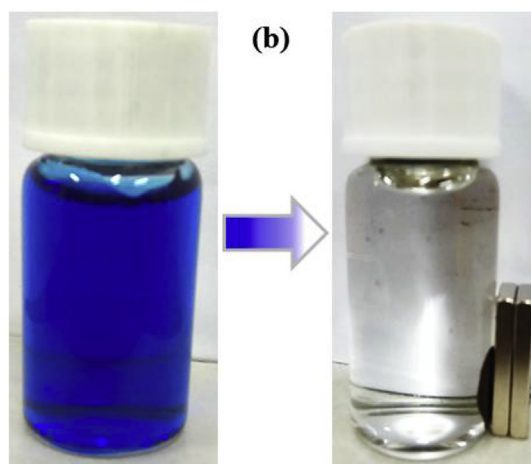
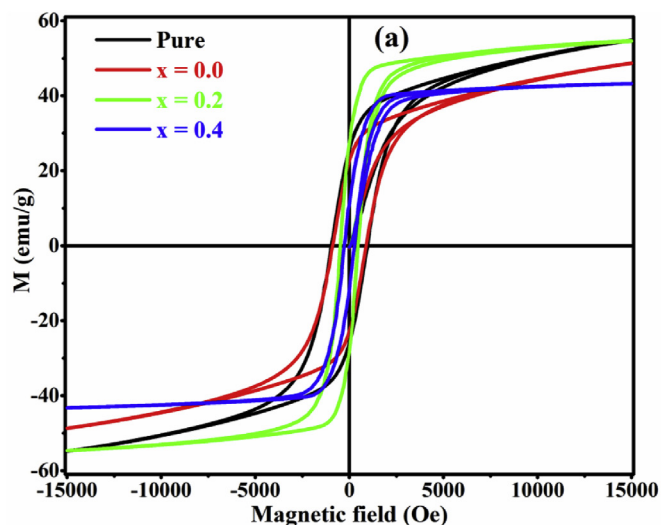


Fig. 10. (a) The variation trend in M – H loops of BASF-NPs and (b) the diagram shows the degradation of MB to water.

experiment i.e. 4, 8, 12 and 16 mM as shown in Fig. 12. Upon employing 16 mM H₂O₂ concentration, complete MB degradation occurred after 140 min in photo-Fenton-like system. It might be attributed to the production of hydroxyl radicals ($\cdot\text{OH}$) as a result of H₂O₂ activation by BASF-NPs catalyst. Furthermore, photo decomposition on BASF-NPs (x = 0.0) surface by forming electron-hole pair (e^-/h^+), or electrons generated in reaction mixture that are immediately trapped by Fe^{3+} and react with H₂O₂ to form Fe^{2+} which can react with H₂O₂ to generate $\cdot\text{OH}$. But, MB degradation efficacy was reduced by using 4, 8 and 12 mM concentration of H₂O₂ and significantly affect the generation of the secondary reactive species, like HO^- , $\text{O}_2^{\cdot-}$, OH_2^- and OH_2^{\cdot} causing a contest among all reactive species existing in reaction mixture. The 16 mM H₂O₂ concentration accelerated the production of oxidizing intermediates which were accountable for MB oxidation. On the other hand, negligible MB degradation was observed in the presence of only H₂O₂ and without BASF-NPs.

Fig. 12. (b) Demonstrates the reaction behavior corresponding to pseudo first order reaction. At neutral pH, the complete degradation was seemed using 0.25 g/L of BASF-NPs (x = 0.0) and 16 mM of H₂O₂ after 140 min reaction. This reflects a substantial enhancement in MB degradation with regard to photo-catalytic system. As shown in Fig. 12. (b) The result of MB degradation data fitting by

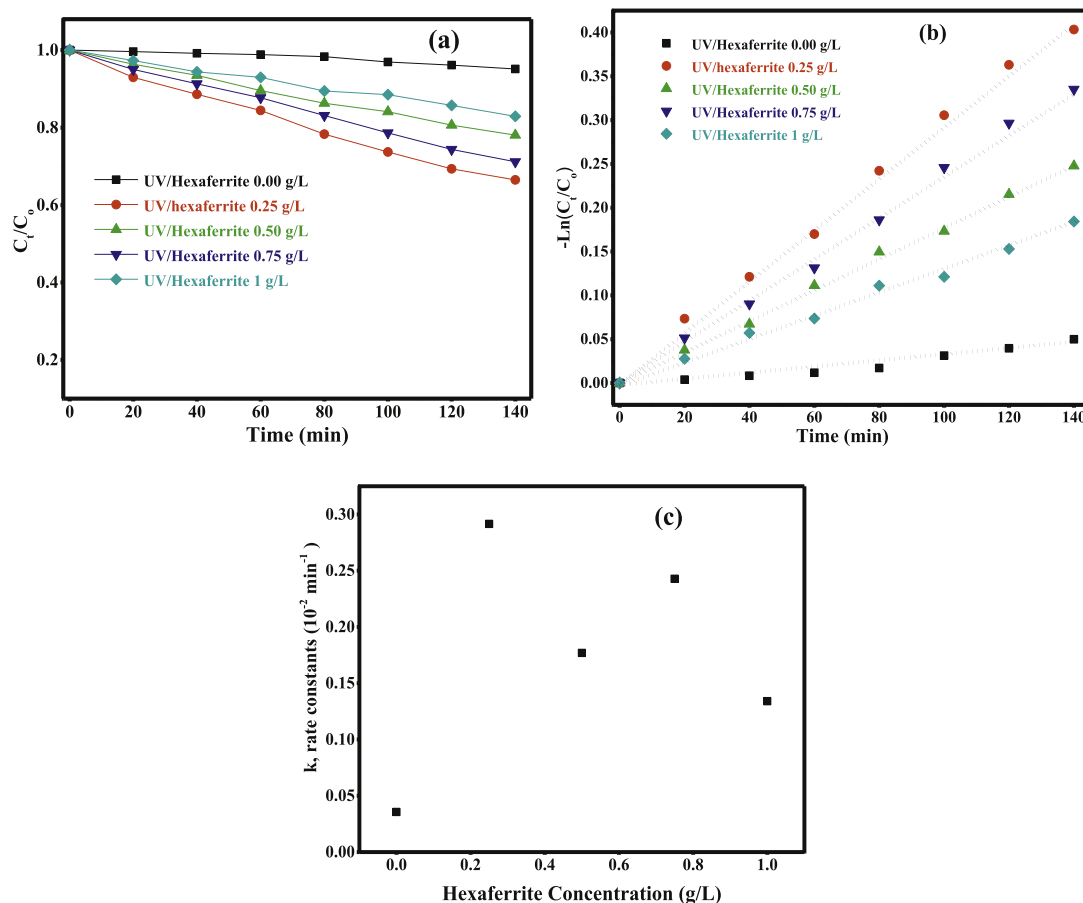


Fig. 11. (a) Effect of different concentration of BASF-NPs ($x = 0.0$) for MB photo degradation (b) pseudo first order linear transformation (c) The rate of reaction constant of BASF-NPs ($x = 0.0$) loading at room temperature.

means of pseudo-first-order kinetic with R^2 value of 0.99. The pseudo-first order kinetic rate constants were $k = 2.66, 3.164, 3.218$ and $6.514 \times 10^{-2} \text{ min}^{-1}$ with respect to 4, 8, 12 and 16 mM H_2O_2 concentration, respectively as revealed in Fig. 12. (c).

The photo-Fenton-like catalytic performances of BASF-NPs (Pure, $x = 0.0, 0.2$, and 0.4) for MB degradation are revealed in Fig. 13. In the presence of UV irradiation and H_2O_2 9.99% MB degradation was achieved without catalyst. MB degradation was attained $\sim 100\%$ for pure sample ($\text{Ba}_{0.4}\text{Sr}_{0.6}\text{Fe}_{12}\text{O}_{19}$) and $x = 0.2$ after 140 min. Such results specified that, relative to $x = 0.0$ and 0.4 nanoparticles, the pure sample and $x = 0.2$ displayed the highest photo Fenton-like activity. TEM micrographs, UV-Vis spectra and BET analysis can explain the higher catalytic activity of the pure and $x = 0.2$. In Fig. 7, TEM micrographs are displayed and the platelet-like hexagonal structure of the pure sample and $x = 0.2$ are observed with larger particle size as shown in Table S1. The comparatively narrow energy band gap was achieved as presented in Fig. 8. The pure samples ($5.85 \text{ m}^2/\text{g}$) and $x = 0.2$ ($8.26 \text{ m}^2/\text{g}$) displayed a larger area than the remaining samples as revealed in Fig. 9. While under optimal condition, MB degradation was achieved about 45% in the dark (without UV light/ H_2O_2 /BASF-NPs) which is due to lack of the electron-hole pairs ($e_{CB} + h_{VB}$) were not produced on BASF-NPs surface [49]. Valero et al. [12] reported pure barium M-hexaferrite $\text{BaFe}_{12}\text{O}_{19}/\text{H}_2\text{O}_2/\text{vis}$ -light can decompose about 70.8% degradation and without vis-light dye degradation is quite lower. Wang et al. [37] attained 95.8% degradation in 100 min with 16.8 wt% $\text{BaFe}_{12}\text{O}_{19}/\text{g}-\text{C}_3\text{N}_4$ composites having lamellar

shaped particle size $\sim 6-7 \mu\text{m}$. It showed that the substitution played a significant part for the present study for degradation of MB as well as size and shape of the particles. The best performance was attained at pure sample and $x = 0.2$ with photo-catalyst concentration 0.25 g/L, 10 mg/L of MB, 16 mM of H_2O_2 and under UV irradiation about ~ 100 and 99% degradation, respectively after 140 min at neutral pH (7) as shown in Table 1.

Fig. 13 (b) demonstrates the pseudo first order reaction behavior. This significantly enhances MB degradation efficiency substituted M-hexaferrite photo-catalytic system. As illustrated in Fig. 13 (b), pseudo-first-order kinetic model with R^2 value of 0.99 of MB degradation data. The pseudo-first order kinetic rate constants are $k = 6.52, 3.16, 5.09$ and $3.22 \times 10^{-2} \text{ min}^{-1}$ with respect to (Pure, $x = 0.0, 0.2$ and 0.4) BASF-NPs as revealed in Fig. 13 (c).

The comparative study of dyes degradation is presented in Table 1 by using various ferrite nanoparticles. The degradation of dye is associated on type of nano-particles, size and morphology. In the present study, BASF-NPs were used for the first time and removed $\sim 100\%$ MB with an optimum 0.25 g/L photo-catalyst. Diao et al. [50] explored MgFe_2O_4 magnetic NPs for dye degradation efficiency of about 96.8% having spherical shaped particles of size 93 nm under UV light within 180 min. Valero et al. [12] synthesized photo-catalyst $\text{BaFe}_{12}\text{O}_{19}$ M-hexaferrite for dye degradation (70.8%) in the existence of H_2O_2 and vis irradiation in 360 min. Xing et al. [10] reported MgFe_2O_4 as a catalyst and achieved 97.8% degradation of dye at given circumstances such as pH 6.44, dosage of catalyst 0.625 g L^{-1} and 1.0 vol% H_2O_2 in 300 min. Fatemeh and co-

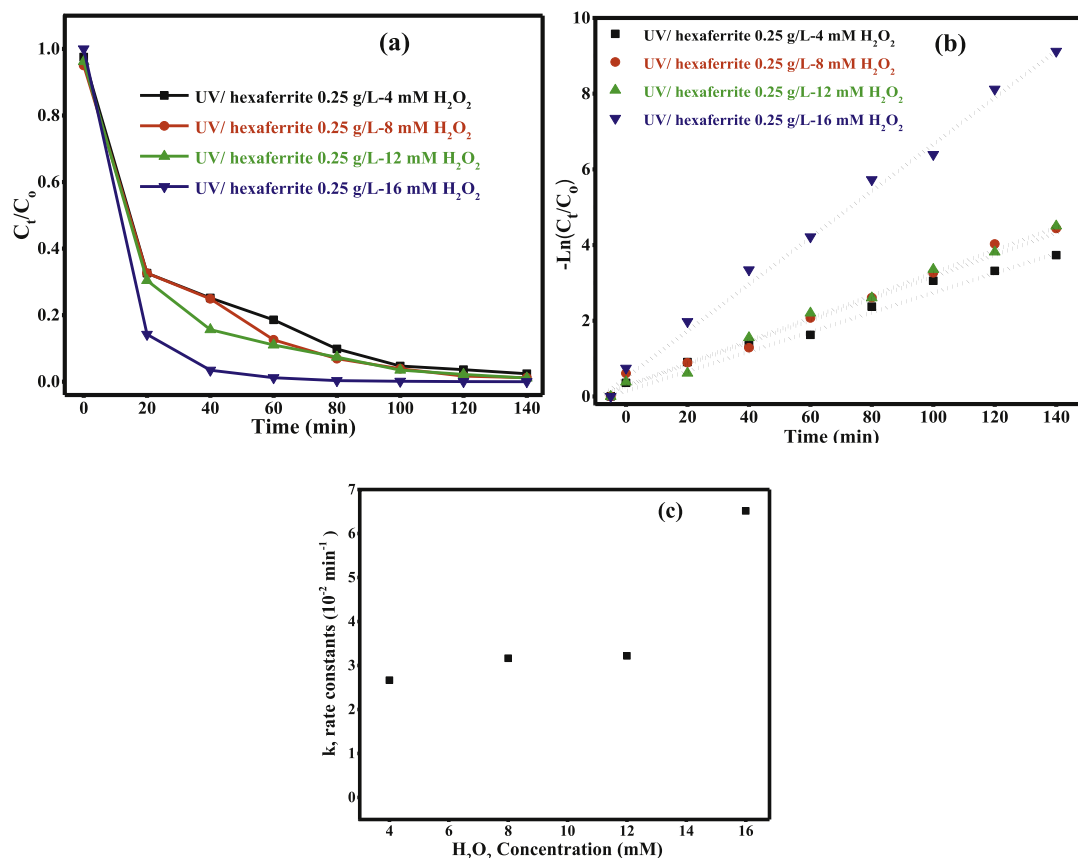


Fig. 12. (a) Effect of different concentration of H_2O_2 (4–16 mM) and 0.25 g/L of BASF-NPs ($x = 0.0$) for photo-Fenton-like degradation of MB (b) pseudo first order linear transformation (c) The reaction rate constant.

researchers synthesized $SrFe_{12}O_{19}@SiO_2@TiO_2$ having sporadic hexagonal shape and their particles estimated size 122 nm and applied photo-catalysts which exposed 80% degradation of MB within 180 min [14]. Wang et al. [37] fabricated 16.8 wt% $BaFe_{12}O_{19}/g-C_3N_4$ (polymeric) nanocomposites for dye degradation in presence of UV light/ H_2O_2 . The degradation was attained about 95.80% under UV irradiation and 56.60% without light irradiation in 100 min. Debesh et al. [51] introduced $SrFe_{12}O_{19}$ having plate-like particles shape and energy band gap 1.70 eV for MB degradation in the presence of visible light, MB degradation was achieved 95% with 270 min.

3.2.3. Impact of pH

Mostly, pH range adjustment assumes a significant job in HC Fenton reaction since this parameter determines the generation rate of hydroxyl radicals. Fig. 14 displays that after 140 min, ~100% degradation of MB dye by pure sample ($Ba_{0.4}Sr_{0.6}Fe_{12}O_{19}$) photo-catalyst was optimally achieved at pH 7. The oxidative volume of hydroxyl radicals was inclined to decline due to a decrease in the oxidation potential of hydroxyl radicals, which resulted in degradation efficacy up to 91.96% at pH 12 [52]. While at lower pH 3 about 95.61% degradation was achieved which may be ascribed protonating H_2O_2 and disfavoring the formation of hydroxyl radicals [53]. It can be clearly observed that $Ba_{0.4}Sr_{0.6}Fe_{12}O_{19}$ photo-catalyst is relatively comparable to further reported photo-catalysts whether catalyst concentration and reaction time [12,14,37]. Hence, $Ba_{0.4}Sr_{0.6}Fe_{12}O_{19}$ and $x = 0.2$ are potential photo-catalysts in the photo-Fenton-like system which establishes the excellent degradation of MB within less time and catalyst

concentration required. This finding verified $Ba_{0.4}Sr_{0.6}Fe_{12}O_{19}$ and $x = 0.2$ photo-catalyst endured stable over a wide pH range. Further the extra change of pH esteems by acidification of treated waters could be sidestepped.

3.2.4. MB concentration

The different primary MB concentrations such as 10, 20 and 30 mg/L was selected to measure MB degradation with this optimal condition (0.25 g/L of pure sample; $Ba_{0.4}Sr_{0.6}Fe_{12}O_{19}$ and 16 mM of H_2O_2 under UV irradiation). At MB concentrations of 10, 20 and 30 mg/L, 99%, 75% and 50% degradation were attained, respectively (Fig. 15). The degradation efficiency slows down at higher concentration of MB due to MB adsorption on photo-catalyst surface may reach saturation level. The transferred electrons to photo-catalyst surface was intervened by adsorbed MB [54]. Additionally, on the photo-catalyst surface the produced intermediates and MB could compete with each other for limited reactive sites, hence inhibiting the overall degradation of MB. It is accepted that increase of MB concentration influences light infiltration throughout the solution. The level of light infiltration at high beginning concentrations is diminished which will result the reaching of fewer photons at the surface of catalyst [55].

3.2.5. Proposed degradation pathway of MB

The accumulation, generation and degradation of MB molecules by photo-Fenton-like process in pure sample/ H_2O_2 /UV system were monitored by UPLC-MS analysis. The chromatograms of generated intermediates as a function of reaction-time are presented in Fig. 16. It can be clearly observed that generated intermediates were

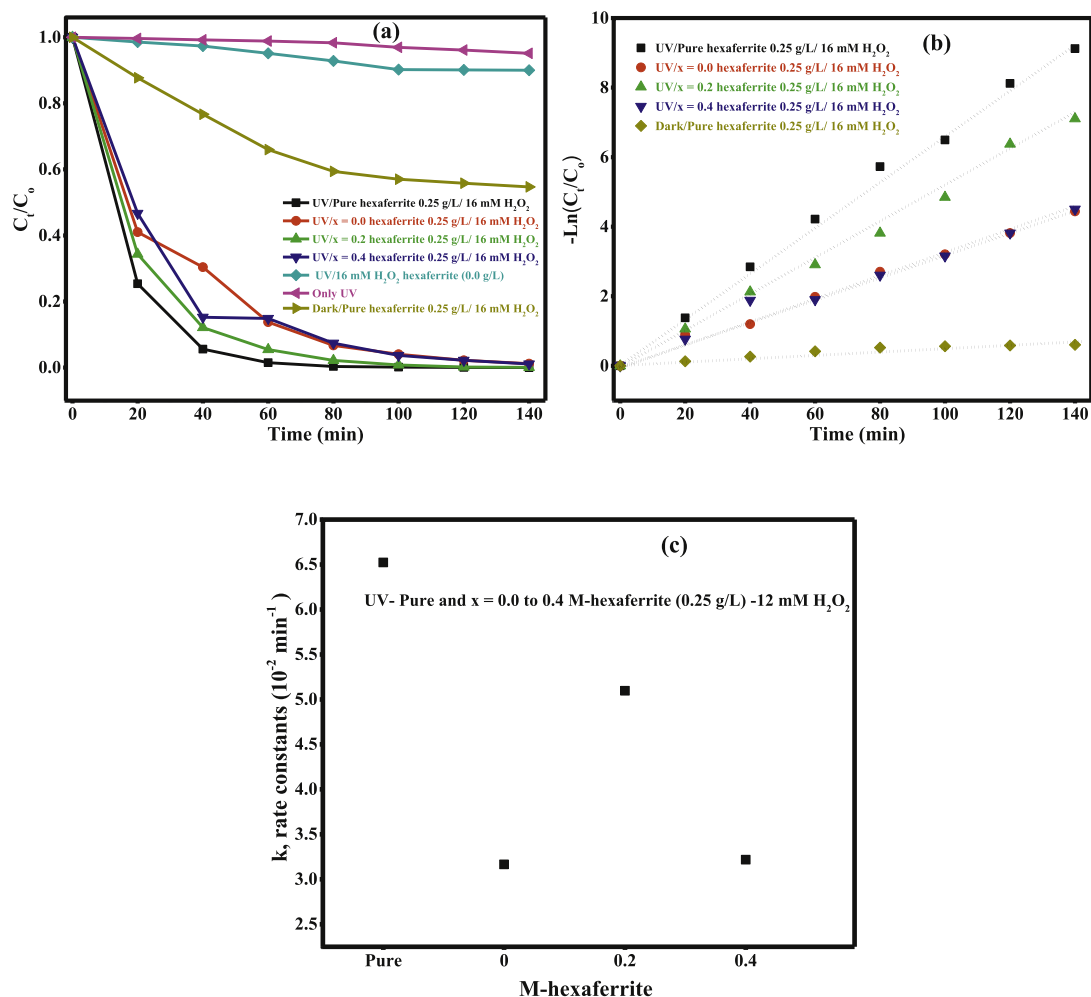


Fig. 13. (a) Effect of BASF-NPs (pure sample, $x = 0.0, 0.2$ and 0.4) having concentration 0.25 g/L , $16 \text{ mM H}_2\text{O}_2$ for photo-Fenton-like degradation of MB (b) pseudo first order linear transformation (c) The reaction rate constant.

Table 1

Comparative analysis of photo-degradation of MB for various BASF-NPs photo-catalysts, Present work: PW.

Oxidation system	Reaction parameters	Degradation efficiency (%)	Ref.
$\text{Ba}_{0.4}\text{Sr}_{0.6}\text{Fe}_{12}\text{O}_{19}$ (pure)/ H_2O_2 /UV Light	10 mg/L of MB; Hexaferrite (0.25 g/L); H_2O_2 (16 mM); reaction time (140 min)	~ 100	PW
$x = 0.0/\text{H}_2\text{O}_2$ /UV light		98.8	PW
$x = 0.2/\text{H}_2\text{O}_2$ /UV light		99	PW
$x = 0.4/\text{H}_2\text{O}_2$ /UV light		98	PW
$\text{MgFe}_2\text{O}_4/\text{H}_2\text{O}_2$ /Vis light	RhB (10 mg/L); catalyst (1 g/L); 1% of H_2O_2 ; reaction time (180 min)	96.8%	[50]
$\text{BaFe}_{12}\text{O}_{19}/\text{H}_2\text{O}_2$ /Vis light	MB (10 mg/L); catalyst (0.75 g/L); 12 mM of H_2O_2 ; reaction time (360 min)	70.8	[12]
$\text{SrFe}_{12}\text{O}_{19}/\text{SiO}_2/\text{TiO}_2$ /UV light	MB (50 mg/L); catalyst (0.03 g/L); reaction time (180 min)	80	[14]
$16.8 \text{ wt}\%$ $\text{BaFe}_{12}\text{O}_{19}/\text{g-C}_3\text{N}_4/\text{H}_2\text{O}_2$ /Vis light	Tetracycline and RhB (10 mg/L); catalyst (1 g/L); 0.5 mL of H_2O_2 reaction time (100 min)	95.8	[37]
BaFe_2O_4 /UV light	Methyl orange (20 mg/L); catalyst (5 g/L); reaction time (120 min)	90	[64]
$\text{NiFe}_{2-x}\text{Al}_x\text{O}_4$ /Visible light	MB ($5 \text{ ppm}/100 \text{ mL}$); catalyst ($40 \text{ mg}/100 \text{ mL}$); reaction time (120 min)	82.58	[65]
10% $\text{BaFe}_{12}\text{O}_{19}/\text{Ag}_3\text{PO}_4$	BPA (20 mg/L); 70 mg of catalyst; Xe arc lamp; reaction time (120 min)	79.8	[66]
$\text{SrFe}_{12}\text{O}_{19}$ /Visible light	MB (10.0 ppm); catalyst (1 g/L); reaction time (270 min)	95	[51]

transformed further and degraded in 140 min. The proposed mechanism of degradation is presented in Fig. 16 following two paths.

For the MB only, a strong signal appeared at $m/z = 284$ which links to dye solution. Based on the generation of sulfate ion SO_4^{2-} and nitrate ion NO_3^- , the predominant suggested mechanism followed by the oxidation of $\text{C-S}^+=\text{C}$ group thionine ring into two paths. Path A followed by the oxidation of dimethylamino group

which generate different intermediates at $m/z = 226, 198, 230, 203$. The peak at $m/z = 203$ indicates the breakdown of thionine ring by releasing sulfur dioxide which boost the opening of phenothiazine heterocyclic structure. The peak at $m/z = 94$ specified the removal of NO_2 from relative parent molecule. The phenolic group further degraded and transformed into inorganic molecules, such as H_2O and CO_2 which represents a comprehensive photocatalytic degradation of MB accelerated by $\cdot\text{OH}$ radicals.

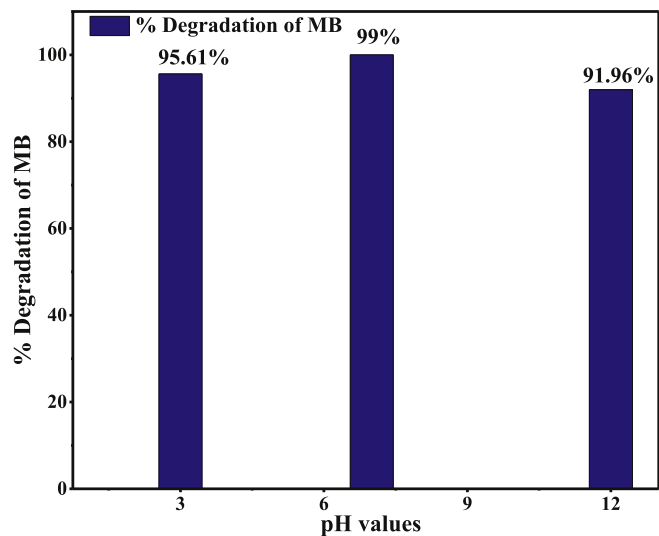


Fig. 14. The influence of pH (3, 7 and 12) on MB degradation with conditions: UV, 0.25 g/L of pure sample; $\text{Ba}_{0.4}\text{Sr}_{0.6}\text{Fe}_{12}\text{O}_{19}$, 16 mM H_2O_2 and 10 mg/L of MB after 140 min.

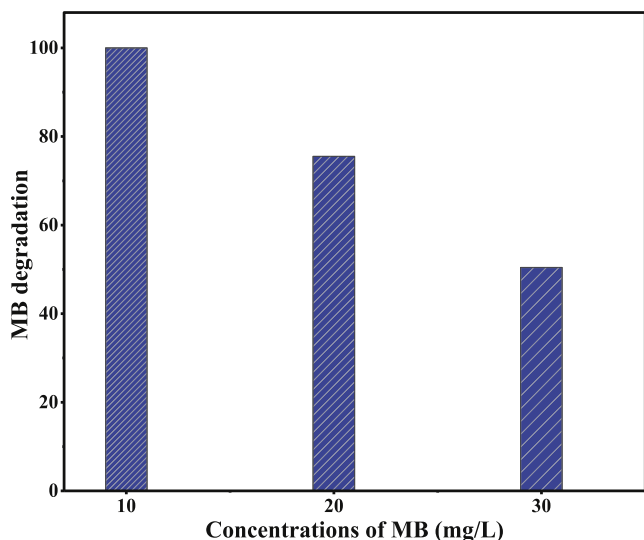


Fig. 15. Impact of initial MB concentration (10, 20 and 30 mg/L) on MB degradation under optimum condition at pH 7 after 140 min.

For instance, the demethylation reaction proved the maximum absorption peaks from parent MB molecules by the blue-shifts accompanying the many intermediated peaks at $m/z = 348$, 189, 125, 109 as resented in mechanism scheme by path B. The formation of different intermediates indicates the variation in the concentration and composition of degradation products. The peak appeared at $m/z = 348$ is because of the hydroxylation of parent MB molecule by replacement of dimethylamino groups. The scission of central ring lead to generate peaks at $m/z = 189$, 124 accordingly. Furthermore, the desulphonation reaction of scission products produced diols and then phenol. Fig. S2 presented to intermediate fragments generated during degradation reaction. After 60, and 120 min appearance of sharp signals represent the presence of oxidative byproducts. The small low intensity peaks show the generation of inorganic fragments having low molecular weight like CO_2 and H_2O , which reveal the MB was degraded completely over time [56].

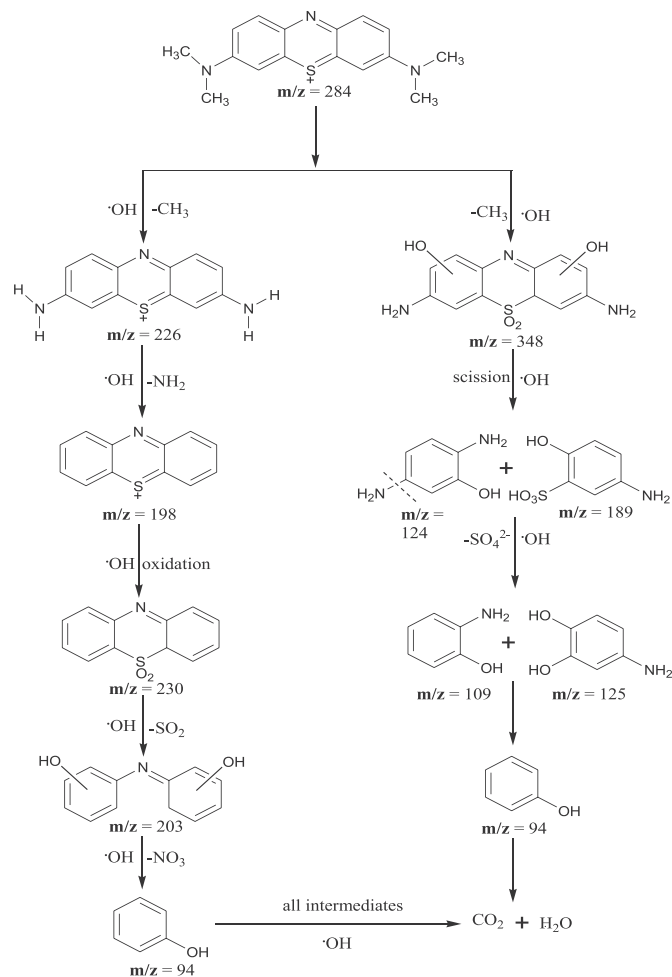


Fig. 16. Proposed degradation reaction mechanism of MB by using pure sample; $\text{Ba}_{0.4}\text{Sr}_{0.6}\text{Fe}_{12}\text{O}_{19}$ (0.25 g/L), 16 mM of H_2O_2 under UV irradiation.

3.2.6. Total organic carbon (TOC)

To explore the mineralization of MB catalyzed by utilizing TOC analyzer. The maximum mineralization of MB (10 mg/L) was attained about 89.85% by using pure sample (0.25 g/L), 16 mM of H_2O_2 under UV irradiation which exhibited a high catalytic activity as shown in Fig. 17. Conversely, less mineralization of MB was seemed with similar comparable amounts of further catalysts under optimum condition. Such as, 79.71, 77.09 and 88.5% mineralization efficiencies were found in the cases of $x = 0.0$, 0.2, and 0.4, respectively. The possible accumulation of dead-end metabolites or intermediate products of MB might be responsible for the partial mineralization of MB as compared to their total degradation.

3.2.7. Recyclability and leaching of BASF-NPs

A persistent issue of photo-catalysts is its reusability. BASF-NPs stability is attributed in the real implementation with long-term reusability. Four cycles of MB degradation were performed to explore pure sample photo-catalyst effect at optimal conditions. Photo-catalyst was removed easily by applying external magnet, washed five time with fresh water and then dried in oven at 150°C after completing each cycle. For each next cycle recovered photo-catalyst concentration was added in water under same optimal conditions. As presented in Fig. 18, after 140 min, the removal of MB for four cycles were 99%, 98.96%, 98.94 and 98.90%, respectively. Hexaferrite photo-catalyst was not showed any significant least

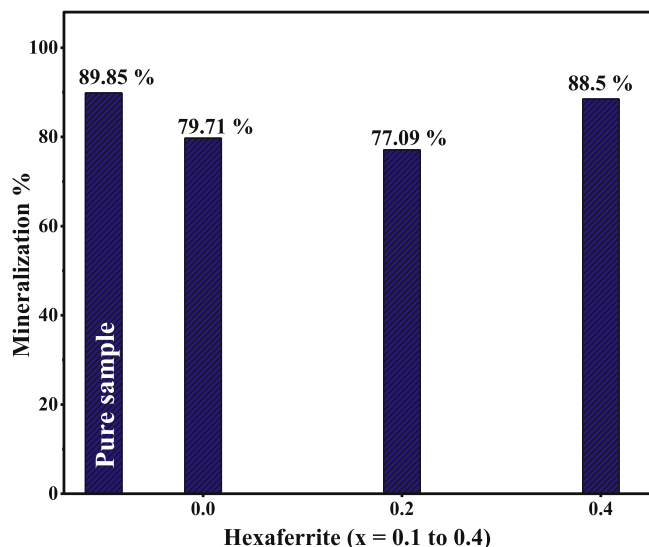


Fig. 17. TOC analysis for BASF-NPs (pure sample; $\text{Ba}_{0.4}\text{Sr}_{0.6}\text{Fe}_{12}\text{O}_{19}$, $x = 0.0, 0.2$ and 0.4) photo-catalysts after 140 min.

performance after four cycles, which revealed the elevated strength and endorsing their commitment for water pollution treatment. The FTIR examination of used NPs after four cycles, also revealed that there were no apparent structural and chemical changes in both fresh and used samples. This investigates an excellent stability of presented photocatalyst (Fig. S3).

During the implementation of HC photo-catalysts, major concern must be paid to the issue of ion leaching. The leaching of Ba, Sr, Al, Sm and Fe ions from the surface of the photo-catalyst was explored after 140 min of MB treated solution after first cycle under optimal condition. In present study, the level of leached Ba, Sr, Al, Sm and Fe ions in the solution approximately was obtained 0.001, 0.003, 0.00, 0.00 and 0.001 mg/L, respectively. There was a very minor leaching in BASF-NPs photo-catalyst. The catalytic impact of such a minor leached ions concentration that further demonstrates HC catalytic reaction happens on BASF-NPs photo-catalyst surface. Similarly Xiao et al. [57] reported that the degradation of MB by

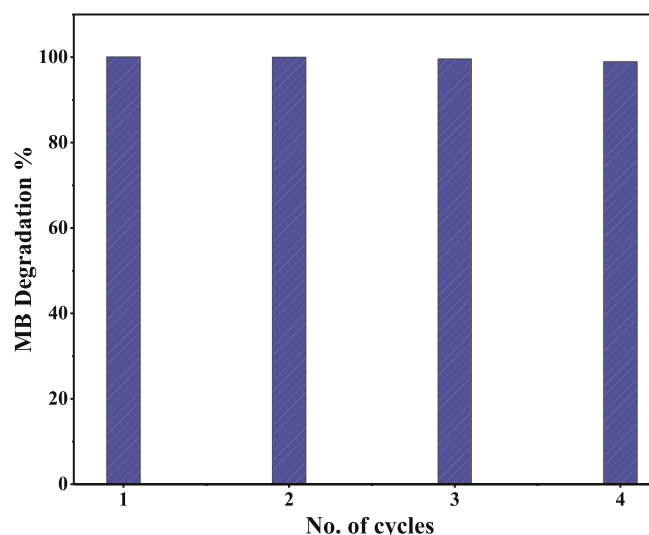


Fig. 18. Operational life of pure sample; $\text{Ba}_{0.4}\text{Sr}_{0.6}\text{Fe}_{12}\text{O}_{19}$ photo-catalyst (0.25 g/L), 16 mM of H_2O_2 under UV irradiation system at neutral pH.

hydroxyl radicals triggered the decomposition of H_2O_2 catalyzed by HC photo-catalyst.

3.2.8. Photocatalytic mechanism in BASF-NPs system

To explore the reactive species contribution to MB degradation mechanism in BASF-NPs/ H_2O_2 /UV irradiation system. The hydroxyl radical's production was assessed by fluorescence technique and terephthalic acid (TA) was used as a probe during the degradation phase. The fluorescence spectra were generated between 340 and 550 nm. From Fig. S4, the active photo-generated hydroxyl radicals were in HC photo-Fenton-like system. At 460 nm the fluorescence signal enhanced by increasing the time which clearly show TA reaction with $\cdot\text{OH}$ and formed 2-hydroxylterephthalic acid. The maximum intensity of fluorescence is associated directly with the amount of $\cdot\text{OH}$ radicals [57,58]. BASF-NPs as a HC photocatalyst show that generated $\cdot\text{OH}$ species play a significant role in this system.

MB degradation mechanism by ($x = 0.2$) BASF-NPs/ H_2O_2 /UV irradiation system at neutral pH (7) as shown in Fig. 19. Normally, HC catalyst system require mass transfer of pollutants to the surface of the catalyst [59]. While in the presence of UV light, the absorbance of photo energy from UV light, the electron-hole pairs ($e_{\text{CB}}^- + h_{\text{VB}}^+$) were produced on ($x = 0.2$) BASF-NPs surface (Eq. (5)) [49]. The BASF-NPs ($x = 0.2$) photo Fenton-like reaction enhancement could be due to Al-Sm substitution being able to accelerate electron transfer production by enhancing the interface between H_2O_2 , and Fe^{3+} resulting in more $\cdot\text{OH}$ radical ensuing from a high rate of H_2O_2 decomposition [60]. XPS valance band spectra of sample ($x = 0.2$) was depicted in Fig. S5 for the determination of the valance band energy (VB). The measured VB energy is positioned at 3.10 eV, while the band gap ($E_g = 1.74$ eV) was calculated in Fig. 8 ($x = 0.2$). As stated by this given equation ($E_{\text{CB}} = E_{\text{VB}} - E_g$), the conduction band energy ($E_{\text{CB}} = 1.36$ eV) was measured [61]. Definitely, BASF-NPs would easily have excited in the presence of UV light due to narrow band gap ultimately the photo electron-hole pairs ($e_{\text{CB}}^- + h_{\text{VB}}^+$) were generated. The photo-electrons at CB could respond with oxygen molecule and reduce it to superoxide radical anion. Also, photo-electrons were produced OH^- ions and $\cdot\text{OH}$ radical in the presence of H_2O_2 . The holes (h_{VB}^+) react with H_2O and OH^- ions in the presence of hexaferrites to generate $\cdot\text{OH}$ radical (Eq. (6)) or direct oxidation. These active species like (O_2^- , $\cdot\text{OH}$ and h_{VB}^+) are liable for MB molecule degradation having some other products, CO_2 and water [62,63]. The suggested photocatalytic degradation mechanism for BASF-NPs may be presented as follows;

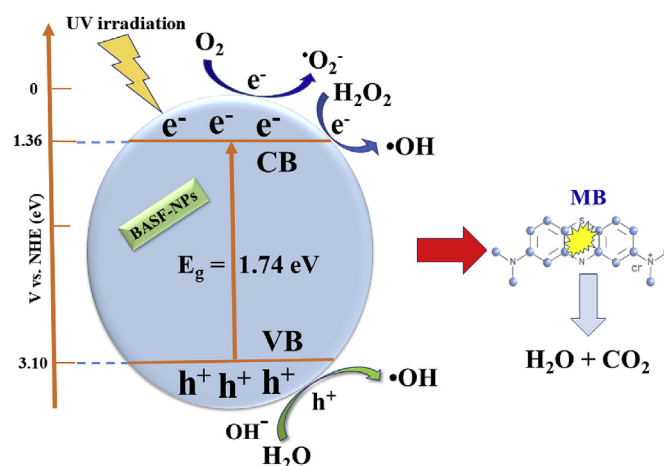
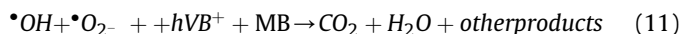
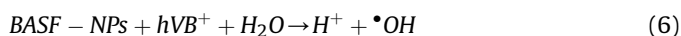


Fig. 19. The MB degradation mechanism by BASF-NPs under UV light.



Hence, the enhanced MB degradation and mineralization would be seemed through the oxidation by $\bullet O_2^-$, $\bullet OH$ and $h\nu B^+$ radicals formed in BASF-NPs/ H_2O_2 /UV irradiation system.

4. Conclusions

M-hexaferrite $Ba_{0.4}Sr_{0.6}Al_{0.4-x}Sm_xFe_{11.60}O_{19}$ (BASF-NPs; pure, $x = 0.0, 0.2$ and 0.4) with strong intrinsic magnetic behavior were successfully characterized and fabricated via sol-gel technique. BASF-NPs were introduced for MB degradation as heterogeneous photo Fenton-like catalyst. In H_2O_2 /BASF-NPs/UV irradiation system, BASF-NPs was able to produce hydroxyl radicals by dissociation of H_2O_2 under UV irradiation. At an optimum 0.25 g/L of pure sample dose and 16 mM H_2O_2 concentration the MB degradation and mineralization was about $\sim 100\%$ and 89.85% , respectively. The reusability and stability of BASF-NPs demonstrated excellent photo Fenton like catalyst activity. The presented finding may lead to the prospective heterogeneous photo Fenton catalyst for organic pollutants treatment.

Author contribution

Ghulam Abbas Ashraf: Major experiments have been carried out in the manufacture of nanoparticles and experimental application and writing. Raqiqa Tur Rasool: The chromatograms of the generated intermediates as a function of the reaction time have been completed. Muhammad Hassan: The work's novelty is established and directed. Lanting Zhang: The work's novelty is established, directed and supported financially.

Declaration of competing interest

The authors declare that there are no conflicts of interest.

Acknowledgments

Acknowledgement This work was supported in part by National Key Research and development Program of China (Grant No. 2017YFB0701900), and the Science Technology Commission of Shanghai Municipality (Grant Nos. 15DZ2260303 and 16DZ2260602).

Appendix A. Supplementary data

Supplementary data to this article can be found online at <https://doi.org/10.1016/j.jallcom.2019.153410>.

References

- [1] S. Mohebbi, D. Bastani, H. Shayesteh, Equilibrium, kinetic and thermodynamic studies of a low-cost biosorbent for the removal of Congo red dye: acid and CTAB-acid modified celery (Apium graveolens), *J. Mol. Struct.* 1176 (2019) 181–193, <https://doi.org/10.1016/j.molstruc.2018.08.068>.
- [2] R.R. Jitta, R. Gundeboina, N.K. Veldurthi, R. Guje, V. Muga, Defect pyrochlore oxides: as photocatalyst materials for environmental and energy applications - a review, *J. Chem. Technol. Biotechnol.* (2015), <https://doi.org/10.1002/jctb.4745>.
- [3] A. Mirzaei, Z. Chen, F. Haghghat, L. Yerushalmi, Removal of pharmaceuticals from water by homo/heterogeneous Fenton-type processes - a review, *Chemosphere* 174 (2017) 665–688, <https://doi.org/10.1016/j.chemosphere.2017.02.019>.
- [4] P.V. Nidheesh, R. Gandhimathi, Degradation of dyes from aqueous solution by Fenton processes: a review, *Environ. Sci. Pollut. Res.* 20 (2013) 2099–2132, <https://doi.org/10.1007/s11356-012-1385-z>.
- [5] R.S. Ribeiro, A.M.T. Silva, J.L. Figueiredo, J.L. Faria, H.T. Gomes, Environmental Catalytic wet peroxide oxidation: a route towards the application of hybrid magnetic carbon nanocomposites for the degradation of organic pollutants. A review, *Appl. Catal. B Environ.* 187 (2016) 428–460, <https://doi.org/10.1016/j.apcatb.2016.01.033>.
- [6] M. Hartmann, H. Keller, Wastewater treatment with heterogeneous Fenton-type catalysts based on porous materials, *J. Mater. Chem.* 20 (2010), <https://doi.org/10.1039/c0jm00577k>, 9002–9017.
- [7] R. Article, *Chem. Soc. Rev.* (2013) 9509–9549, <https://doi.org/10.1039/c3cs60176e>.
- [8] A. Ivanets, M. Roshchina, V. Srivastava, V. Prozorovich, T. Dontsova, S. Nahiriak, V. Pankov, A. Hosseini-Bandegharai, H. Nguyen Tran, M. Sillanpää, Effect of metal ions adsorption on the efficiency of methylene blue degradation onto MgFe 2 O 4 as Fenton-like catalysts, *Colloids Surf. A Physicochem. Eng. Asp.* 571 (2019) 17–26, <https://doi.org/10.1016/j.colsurfa.2019.03.071>.
- [9] Y. Wang, H. Zhao, M. Li, J. Fan, G. Zhao, Magnetic ordered mesoporous copper ferrite as a heterogeneous Fenton catalyst for the degradation of imidacloprid, *Appl. Catal. B Environ.* 147 (2014) 534–545, <https://doi.org/10.1016/j.apcatb.2013.09.017>.
- [10] X. Han, H. Zhang, T. Chen, M. Zhang, M. Guo, Facile synthesis of metal-doped magnesium ferrite from saprolite laterite as an effective heterogeneous Fenton-like catalyst, *J. Mol. Liq.* 272 (2018) 43–52, <https://doi.org/10.1016/j.molliq.2018.09.045>.
- [11] A.A. Farghali, M.H. Khedr, A.F. Moustafa, Photocatalytic Activity and Magnetic Properties of Nanocrystallite Strontium Hexaferrite Prepared by Self-Flash Combustion, 2013, p. 7857, <https://doi.org/10.1179/175355508X310089>.
- [12] C. Valero-Luna, S.A. Palomares-Sánchez, F. Ruiz, Catalytic activity of the barium hexaferrite with H2O2/visible light irradiation for degradation of Methylene Blue, *Catal. Today* 266 (2016) 110–119, <https://doi.org/10.1016/j.cattod.2015.08.049>.
- [13] M. Li, Q. Gao, T. Wang, Y. Gong, B. Han, K. Xia, C. Zhou, Solvothermal synthesis of Mn_x Fe_{3-x}O₄ nanoparticles with interesting physicochemical characteristics and good catalytic degradation activity, *Mater. Des.* 97 (2016) 341–348, <https://doi.org/10.1016/j.matdes.2016.02.103>.
- [14] F. Bavarsih, M. Rajabi, M. Montazeri-Pour, Synthesis of SrFe₂O₄/SiO₂/TiO₂ composites with core/shell/shell nano-structure and evaluation of their photo-catalytic efficiency for degradation of methylene blue, *J. Mater. Sci. Mater. Electron.* 29 (2018) 1877–1887, <https://doi.org/10.1007/s10854-017-8098-5>.
- [15] X. Guo, D. Wang, Photo-Fenton degradation of methylene blue by synergistic action of oxalic acid and hydrogen peroxide with NiFe₂O₄ hollow nanospheres catalyst, *J. Environ. Chem. Eng.* 7 (2019), <https://doi.org/10.1016/j.jece.2018.102814>, 102814.
- [16] M. Danish, X. Gu, S. Lu, M.L. Brusseu, A. Ahmad, M. Naqvi, U. Farooq, W. Qamar, X. Fu, Z. Miao, Applied Catalysis A: general an efficient catalytic degradation of trichloroethene in a percarbonate system catalyzed by ultra-fine heterogeneous zeolite supported zero valent iron-nickel bimetallic composite, *Appl. Catal. Gen.* 531 (2017) 177–186, <https://doi.org/10.1016/j.apcata.2016.11.001>.
- [17] N. Panda, H. Sahoo, S. Mohapatra, Decolorization of methyl orange using Fenton-like mesoporous Fe₂O₃-SiO₂ composite, *J. Hazard Mater.* 185 (2011) 359–365, <https://doi.org/10.1016/j.jhazmat.2010.09.042>.
- [18] L. Xu, J. Wang, Environmental Fenton-like degradation of 2, 4-dichlorophenol using Fe₃O₄ magnetic nanoparticles, *Appl. Catal. B Environ.* 123–124 (2012) 117–126, <https://doi.org/10.1016/j.apcatb.2012.04.028>.
- [19] X. Li, Y. Huang, C. Li, J. Shen, Y. Deng, Degradation of p CNB by Fenton like process using a -FeOOH, *Chem. Eng. J.* 260 (2015) 28–36, <https://doi.org/10.1016/j.cej.2014.08.042>.
- [20] Y. Feng, C. Liao, K. Shih, Copper-promoted circumneutral activation of H₂O₂ by magnetic CuFe₂O₄ spinel nanoparticles: mechanism, stoichiometric efficiency, and pathway of degrading sulfanilamide, *Chemosphere* 154 (2016) 573–582, <https://doi.org/10.1016/j.chemosphere.2016.04.019>.
- [21] L. Zhang, D. Xu, C. Hu, Y. Shi, Framework Cu-doped AlPO₄ as an effective Fenton-like catalyst for bisphenol A degradation, *Appl. Catal. B Environ.* 207 (2017) 9–16, <https://doi.org/10.1016/j.apcatb.2017.02.002>.
- [22] R.C. Pullar, Hexagonal ferrites: a review of the synthesis, properties and

- applications of hexaferrite ceramics, *Prog. Mater. Sci.* 57 (2012), <https://doi.org/10.1016/j.pmatsci.2012.04.001>, 1191–1334.
- [23] M. Javed, M. Naem, P. Hernandez, Effect of doping of Zr – Zn binary mixtures on structural , electrical and magnetic properties of Sr-hexaferrite nanoparticles, *J. Alloy. Comp.* 478 (2009) 736–740, <https://doi.org/10.1016/j.jallcom.2008.11.136>.
- [24] R.A. Pawar, S.S. Desai, Q.Y. Tamboli, S.E. Shirsath, S.M. Patange, Ce³⁺ incorporated structural and magnetic properties of M type barium hexaferrites, *J. Magn. Magn. Mater.* 378 (2015) 59–63, <https://doi.org/10.1016/j.jmmm.2014.10.166>.
- [25] S. Kim, W. Wang, T. Iwaki, A. Yabuki, K. Okuyama, Low-temperature crystallization of barium ferrite nanoparticles by a sodium citrate-aided synthetic process, *J. Phys. Chem.* (2007) 10175–10180, <https://doi.org/10.1021/jp068249b>.
- [26] M.J. Iqbal, S. Farooq, Extraordinary role of Ce – Ni elements on the electrical and magnetic properties of Sr – Ba M-type hexaferrites, *Mater. Res. Bull.* 44 (2009) 2050–2055, <https://doi.org/10.1016/j.materresbull.2009.07.015>.
- [27] T.M. Meaz, M.A. Amer, H.A.E.L. Shersaby, Effect of trivalent ion substitution on the physical properties of M-type hexagonal ferrites, *J. Part. Sci. Technol.* 32 (2014) 39–45, <https://doi.org/10.1080/02726351.2013.793759>.
- [28] G. Abbas, L. Zhang, W. Abbas, G. Murtaza, Synthesis and characterizations of Al-Sm substituted Ba-Sr M-type hexagonal ferrite nanoparticles via sol-gel route, *Ceram. Int.* 44 (2018) 18678–18685, <https://doi.org/10.1016/j.ceramint.2018.07.096>.
- [29] M.J. Iqbal, S. Farooq, Impact of Pr – Ni substitution on the electrical and magnetic properties of chemically derived nanosized strontium – barium hexaferrites, *J. Alloy. Comp.* 505 (2010) 560–567, <https://doi.org/10.1016/j.jallcom.2010.06.073>.
- [30] M. Ahmad, R. Grössinger, M. Kriegisch, F. Kubel, M.U. Rana, Magnetic and microwave attenuation behavior of Al-substituted Co 2 W hexaferrites synthesized by sol-gel autocombustion process, *Curr. Appl. Phys.* 12 (2012) 2–9, <https://doi.org/10.1016/j.cap.2012.02.038>.
- [31] S.K. Chawla, S.S. Meena, P. Kaur, R.K. Mudsainiyan, S.M. Yusuf, Effect of site preferences on structural and magnetic switching properties of CO – Zr doped strontium hexaferrite SrCo x Zr x Fe (12 Å 2 x) O 19, *J. Magn. Magn. Mater.* 378 (2015) 84–91, <https://doi.org/10.1016/j.jmmm.2014.10.168>.
- [32] S. Katiakunta, S.S. Meena, S. Srinath, M. Bououdina, R. Sandhya, K. Praveena, Improved magnetic properties of Cr³⁺ doped SrFe₁₂O₁₉ synthesized via microwave hydrothermal route, *Mater. Res. Bull.* 63 (2015) 58–66, <https://doi.org/10.1016/j.materresbull.2014.11.043>.
- [33] T. Xie, C. Liu, L. Xu, J. Yang, W. Zhou, Novel heterojunction Bi₂O₃/SrFe₁₂O₁₉ magnetic photocatalyst with highly enhanced photocatalytic activity, *J. Phys. Chem. C* (2013) 6–15, <https://doi.org/10.1021/jp408627e>.
- [34] M.V. Bukhtiyarova, A.S. Ivanova, E.M. Slavinskaya, L.M. Plyasova, V. V Kaichev, P.A. Kuznetsov, Selective catalytic reduction of nitrogen oxide by ammonia on substituted strontium ferrites, *Appl. Catal. Gen.* 384 (2010) 230–240, <https://doi.org/10.1016/j.apcata.2010.06.046>.
- [35] L. Wang, J. Zhang, Q. Zhang, N. Xu, J. Song, XAFS and XPS studies on site occupation of Sm 3 þ ions in Sm doped, *J. Magn. Magn. Mater.* 377 (2015) 362–367, <https://doi.org/10.1016/j.jmmm.2014.10.097>.
- [36] J. Singh, C. Singh, D. Kaur, H. Zaki, I.A. Abdel-Latif, M. Ghimire, S.E. Shirsath, S.S. Meena, Elucidation of phase evolution, microstructural, Mossbauer and magnetic properties of Co-Al doped M-type Ba-Sr hexaferrites synthesized by a ceramic method, *J. Alloy. Comp.* 695 (2017) 1112–1121, <https://doi.org/10.1016/j.jallcom.2016.10.237>.
- [37] H. Wang, Y. Xu, L. Jing, S. Huang, Y. Zhao, M. He, H. Xu, H. Li, Novel magnetic BaFe₁₂O₁₉/g-C₃N₄ composites with enhanced thermocatalytic and photo-Fenton activity under visible-light, *J. Alloy. Comp.* 710 (2017) 510–518, <https://doi.org/10.1016/j.jallcom.2017.03.144>.
- [38] N. Yasmin, M. Mirza, S. Muhammad, M. Zahid, M. Ahmad, M.S. Awan, A. Muhammad, Influence of samarium substitution on the structural and magnetic properties of M-type hexagonal ferrites, *J. Magn. Magn. Mater.* 446 (2018) 276–281, <https://doi.org/10.1016/j.jmmm.2017.09.005>.
- [39] T. Zeeshan, S. Anjum, S. Waseem, L. Mustufa, Tailoring of structural and magnetic properties by substitution of copper in cobalt chromium ferrites, *Ceram. Int.* 44 (2018) 17709–17715, <https://doi.org/10.1016/j.ceramint.2018.06.235>.
- [40] P. Chavan, L.R. Naik, Investigation of energy band gap and conduction mechanism of magnesium substituted nickel ferrite nanoparticles, *Phys. Status Solidi Appl. Mater. Sci.* 214 (2017) 1–8, <https://doi.org/10.1002/pssa.201700077>.
- [41] J. Qu, T. Che, L. Shi, Q. Lu, S. Qi, A novel magnetic silica supported spinel ferrites NiFe₂O₄ catalyst for heterogeneous Fenton-like oxidation of rhodamine B, *Chin. Chem. Lett.* 30 (2019) 1198–1203, <https://doi.org/10.1016/j.ccllet.2019.01.021>.
- [42] Y. Yang, F. Wang, X. Liu, J. Shao, D. Huang, Magnetic and microstructural properties of Al substituted M-type Ca – Sr hexaferrites, *J. Magn. Magn. Mater.* 421 (2017) 349–354, <https://doi.org/10.1016/j.jmmm.2016.08.034>.
- [43] J. Jiang, L. Li, F. Xu, Y. Xie, Preparation and magnetic properties of Zn – Cu – Cr – Sm ferrite via a rheological phase reaction method, *Mater. Sci. Eng. B* 137 (2007) 166–169, <https://doi.org/10.1016/j.mseb.2006.11.014>.
- [44] W. Abbas, I. Ahmad, M. Kanwal, G. Murtaza, I. Ali, M. Azhar, M. Niaz, M. Ahmad, Structural and magnetic behavior of Pr-substituted M-type hexagonal ferrites synthesized by sol – gel autocombustion for a variety of applications, *J. Magn. Magn. Mater.* 374 (2015) 187–191, <https://doi.org/10.1016/j.jmmm.2014.08.029>.
- [45] J. Singh, C. Singh, D. Kaur, H. Zaki, I.A. Abdel-Latif, S.B. Narang, R. Jotania, S.R. Mishra, R. Joshi, P. Dhruv, M. Ghimire, S.E. Shirsath, S.S. Meena, Elucidation of phase evolution, microstructural, Mössbauer and magnetic properties of Co²⁺ – Al³⁺ doped M-type Ba-Sr hexaferrites synthesized by a ceramic method, *J. Alloy. Comp.* 695 (2017) 1112–1121, <https://doi.org/10.1016/j.jallcom.2016.10.237>.
- [46] L. Wang, J. Zhang, Q. Zhang, N. Xu, J. Song, XAFS and XPS studies on site occupation of Sm³⁺ ions in Sm doped M-type BaFe₁₂O₁₉, *J. Magn. Magn. Mater.* 377 (2015) 362–367, <https://doi.org/10.1016/j.jmmm.2014.10.097>.
- [47] B. Fei, J. Zhong, N. Deng, J. Wang, Q. Liu, Y. Li, X. Mei, A novel 3D heteropoly blue type photo-Fenton-like catalyst and its ability to remove dye pollution, *Chemosphere* 197 (2018) 241–250, <https://doi.org/10.1016/j.chemosphere.2018.01.053>.
- [48] X. Hou, X. Huang, Z. Ai, J. Zhao, L. Zhang, Ascorbic acid/Fe @ Fe 2 O 3 : a highly efficient combined Fenton reagent to remove organic contaminants, *J. Hazard Mater.* 310 (2016) 170–178, <https://doi.org/10.1016/j.jhazmat.2016.01.020>.
- [49] F.L.G.L. Fan, J. Tong, Visible-light-induced photocatalyst based on cobalt-doped zinc ferrite nanocrystals, *Ind. Eng. Chem. Res.* (2012) 13639–13647.
- [50] Y. Diao, Z. Yan, M. Guo, X. Wang, Magnetic multi-metal co-doped magnesium ferrite nanoparticles: an efficient visible light-assisted heterogeneous Fenton-like catalyst synthesized from saprolite laterite ore, *J. Hazard Mater.* 344 (2018) 829–838, <https://doi.org/10.1016/j.jhazmat.2017.11.029>.
- [51] D.D. Mishra, G. Tan, Visible photocatalytic degradation of methylene blue on magnetic SrFe 12 O 19, *J. Phys. Chem. Solids* 123 (2018) 157–161, <https://doi.org/10.1016/j.jpcs.2018.07.018>.
- [52] P. Bautista, A.F. Mohedano, J.A. Casas, J.A. Zazo, J.J. Rodriguez, An overview of the application of Fenton oxidation to industrial wastewaters treatment, *J. Chem. Technol. Biotechnol.* 1338 (2008) 1323–1338, <https://doi.org/10.1002/jctb>.
- [53] A. Gallard, Catalytic decomposition of hydrogen peroxide by Fe (III) in homogeneous aqueous solution : mechanism and kinetic modeling, *Environ. Sci. Technol.* 33 (1999) 2726–2732, <https://doi.org/10.1021/es981171v>.
- [54] H.B. Hadjitaief, P. Da Costa, M.E. Galvez, M. Ben Zina, In fluence of operational parameters in the heterogeneous photo-Fenton discoloration of wastewaters in the presence of an iron-pillared clay, *Ind. Eng. Chem. Res.* 52 (2013) 16656–16665, <https://doi.org/10.1021/ie4018258>.
- [55] B. Zhou, X. Zhao, H. Liu, J. Qu, C.P. Huang, Visible-light sensitive cobalt-doped BiVO₄ (Co-BiVO₄) photocatalytic composites for the degradation of methylene blue dye in dilute aqueous solutions, *Appl. Catal. B Environ.* 99 (2010) 214–221, <https://doi.org/10.1016/j.apcatb.2010.06.022>.
- [56] H. Of, DISSOCIATION, (n.d).
- [57] C. Xiao, J. Li, G. Zhang, Synthesis of stable burger-like a-Fe₂O₃ catalysts : formation mechanism and excellent photo-Fenton catalytic performance, *J. Clean. Prod.* 180 (2018) 550–559, <https://doi.org/10.1016/j.jclepro.2018.01.127>.
- [58] S. Li, I.V. Timoshkin, M. Maclean, S.J. Macgregor, M.P. Wilson, M.J. Given, Fluorescence detection of hydroxyl radicals in water produced by atmospheric pulsed discharges, *IEEE Trans. Dielectr. Electr. Insul.* 22 (2015) 1856–1865, <https://doi.org/10.1109/TDEI.2015.005147>.
- [59] J. Herrmann, Heterogeneous photocatalysis : state of the art and present applications, *Top. Catal.* 34 (2005) 49–64, <https://doi.org/10.1007/s11244-005-3788-2>.
- [60] X.S. Nguyen, G. Zhang, X. Yang, Mesocrystalline Zn-doped Fe₃O₄ hollow submicrospheres: formation mechanism and enhanced photo-Fenton catalytic performance, *ACS Appl. Mater. Interfaces* 9 (2017) 8900–8909, <https://doi.org/10.1021/acsami.6b16839>.
- [61] W. Xie, L. Zhong, Z. Wang, F. Liang, X. Tang, C. Zou, G. Liu, Photocatalytic performance of Bi₂VO_{5.5}/Bi₂O₃ laminated composite films under simulated sunlight irradiation, *Solid State Sci.* 94 (2019) 1–7, <https://doi.org/10.1016/j.solidstatesciences.2019.05.010>.
- [62] S. Kim, W. Choi, Kinetics and mechanisms of photocatalytic degradation of Suspension : the role of OH radicals, *Environ. Sci. Technol.* 36 (2002) 2019–2025, <https://doi.org/10.1021/es015560s>.
- [63] S. Samakchi, N. Chaibakhsh, Z. Moradi-shoeili, Performance in visible light photo-Fenton-like process, *J. Photochem. Photobiol. A Chem.* 367 (2018) 420–428, <https://doi.org/10.1016/j.jphotochem.2018.09.003>.
- [64] Y. Yang, Y. Jiang, Y. Wang, Y. Sun, L. Liu, J. Zhang, Influences of sintering atmosphere on the formation and photocatalytic property of BaFe 2 O 4, *Mater. Chem. Phys.* 105 (2007) 154–156, <https://doi.org/10.1016/j.matchemphys.2007.04.050>.
- [65] M.M. Naik, H.S.B. Naik, G.N.M. Vinuth, K.V.S.K. Rashmi, Effect of aluminium doping on structural , optical , photocatalytic and antibacterial activity on nickel ferrite nanoparticles by sol – gel auto-combustion method, *J. Mater. Sci. Mater. Electron.* 29 (2018) 20395–20414, <https://doi.org/10.1007/s10854-018-0174-y>.
- [66] Y. Xu, F. Ge, M. Xie, S. Huang, J. Qian, H. Wang, M. He, H. Xu, H. Li, Fabrication of magnetic BaFe₁₂O₁₉/Ag₃PO₄ composites with an in situ photo-Fenton-like reaction for enhancing reactive oxygen species under visible light irradiation, *Catal. Sci. Technol.* 9 (2019) 2563–2570, <https://doi.org/10.1039/c8cy02449a>.